Finite element implementation of the thermal field dislocation mechanics model: study of temperature evolution due to dislocation activity

Gabriel Dante Lima-Chaves, Manas V Upadhyay

Finite element implementation of the thermal field dislocation mechanics model: study of temperature evolution due to dislocation activity

Gabriel D. Lima-Chaves, Manas V. Upadhyay*

Laboratoire de Mécanique des Solides (LMS), CNRS UMR 7649, École Polytechnique, Institut Polytechnique de Paris, Route de Saclay, 91120 Palaiseau, France

Abstract

The fully coupled small deformation formulation of the thermal field dislocation mechanics model (Upadhyay (2020)) is numerically implemented using the finite element method. The implementation consists of solving a first-order div-curl system to obtain an incompatible plastic distortion from a prescribed polar dislocation density along with three governing partial differential equations (PDE): the dislocation transport equation (a first-order hyperbolic PDE), the static equilibrium equation (an elliptic PDE), and the temperature evolution equation (a parabolic PDE). A combination of continuous Galerkin (for the elliptic and parabolic PDEs) and discontinuous Galerkin (for the hyperbolic PDE) space discretizations and Runge-Kutta time discretizations are used to implement these equations in a staggered algorithm and obtain stable solutions at (quasi-)optimal convergence rates. The implementation is validated by comparing the simulation-predicted temperature evolution of a moving edge dislocation with an analytical solution. Next, the contribution of plastic dissipation and thermoelastic effect to the temperature evolution during the motion of an edge and a screw dislocation, annihilation of two edge dislocations and expansion of a dislocation loop are studied in detail. In the case of a moving edge dislocation, contrary to existing literature, the thermoelastic effect is demonstrated to have a more significant contribution to temperature evolution than plastic dissipation for the studied traction boundary condition and dislocation velocity expression. In the dislocation loop expansion case, the role of free surfaces on temperature evolution is highlighted. As the loop approaches the free surfaces, plastic dissipation is found to have an increasing contribution to temperature evolution due to the growing impact of image stresses.

Keywords: solids; elasticity; plasticity; thermomechanics; numerical methods; partial differential equations

1. Introduction

The thermal field dislocation mechanics (TFDM) model (Upadhyay (2020)) is a fully coupled dislocation thermomechanics model designed in a small deformation setting to study dislocation evolution under any thermomechanical boundary conditions. TFDM finds its roots in the isothermal field dislocation mechanics (FDM) (Acharya (2001), Acharya (2003)), which is a thermodynamically rigorous model capable of predicting internal stresses due to dislocations, dislocation annihilation, dislocation dynamics in the presence of inertia, considering nonlinear elasticity and/or elastic anisotropy. FDM itself is based on previous works on continuously distributed dislocations (Mura (1963), Willis (1967), Kosevich (1979)). TFDM is able to tackle the aforementioned problems and go beyond the scope of FDM to solve the fully coupled thermomechanical initial boundary value problem with the particular aim of studying those processes that induce strong temperature gradients and heating/cooling rates, such as metal additive manufacturing, welding, quenching, etc.

This paper aims to propose a numerical implementation of the TFDM model using the finite element method (FEM), validate it and present some applications. In the TFDM model, the plastic incompatibility introduced by a prescribed polar dislocation density is expressed by a first-order div-curl system, which is solved using a least squares finite element method (LSFEM) proposed in Roy & Acharya (2005). This approach avoids the issue of having more equations than unknowns when using the conventional continuous Galerkin approach. The static equilibrium equation is an elliptic PDE that is solved by a continuous Galerkin (CG) approximation (Roy & Acharya (2005)). At the core of the model lies the dislocation density evolution equation, a first-order hyperbolic advection-reaction-type PDE, which arises from the statement of conservation of Burgers vector (see Acharya (2011)). Different approaches to solving this equation can be found in the literature, for instance, a weighted CG/LSFEM scheme (Varadhan et al. (2006)) and a fast Fourier transform approach with spectral filters (Djaka et al. (2015)). However, the hyperbolic nature of this PDE leads to solutions for the dislocation density that present discontinuities, hence, discontinuous function spaces are better suited to approximate the solution than continuous approaches. In this regard,

*Corresponding author
Email address: manas.upadhyay@polytechnique.edu (Manas V. Upadhyay)

Upadhyay & Bleyer (2021) proposed a time-explicit 3-dimensional Runge-Kutta discontinuous Galerkin (RKDG) scheme that allows for stable dislocation transport with (quasi)-optimal convergence rates, and is the adopted approach in this work. The temperature evolution equation is a parabolic PDE and is solved using a semi-implicit time discretization and a CG space discretization. Owing to the fully coupled character of the model, the thermoelastic effect and the plastic dissipation due to dislocation evolution are considered in the temperature evolution. To avoid dealing with many degrees of freedom in a monolithic scheme, the FE implementation of these equations is done using a staggered approach.

The structure of this paper is the following: mathematical notation used in this work is presented in Section 2; the TFDM model is briefly described in Section 3; the approximation of the model using the FEM is described in Section 4, in which an algorithm is also proposed; in Section 5, the main results of this work are discussed, including the comparison of the model-predicted temperature evolution with the one obtained from an analytical solution; then, the temperature profiles generated by the motion of an edge and a screw dislocation, dislocation annihilation and loop expansion are studied in detail; the concluding remarks are presented in Section 6.

2. Notations

Scalars are denoted with an italic font (e.g., r or θ). Vectors are denoted by a lowercase bold and italic font (e.g., $\boldsymbol{q}$). Unit vectors are identified by an additional overhead hat symbol $\hat{\square}$. Second-order tensors are denoted by an uppercase bold and italic font or by bold and italic Greek letters (e.g., $\boldsymbol{U}$ or $\boldsymbol{\alpha}$). The second-order identity tensor is written as $\mathbb{1}$, whose components are δ_{ij} (the Kronecker delta). The third-order Levi-Civita permutation tensor is denoted by $\mathbf{X}$, with components e_{ijk} (the permutation symbol). Fourth-order tensors are denoted by double-stroke letters (e.g., $\mathbb{C}$). The null tensor is denoted 0 for any tensor order. Consider two vectors $\boldsymbol{u}$ and $\boldsymbol{v}$, two second-order tensors $\boldsymbol{\alpha}$ and $\boldsymbol{B}$, and a fixed Cartesian reference frame with orthonormal basis $\{\hat{\boldsymbol{e}}_i\}$, $i = 1, 2, 3$ in the x, y and z-directions, respectively. Adopting Einstein notation, the following operations are used in this work (all subscripts below range from 1 to 3):

Tensor product: $\boldsymbol{u} \otimes \boldsymbol{v} = u_i v_j \, \hat{\boldsymbol{e}}_i \otimes \hat{\boldsymbol{e}}_j$

Inner product: $\boldsymbol{u} \cdot \boldsymbol{v} = u_i v_i$

$\boldsymbol{\alpha} : \boldsymbol{B} = \alpha_{ij} B_{ij}$

Cross product: $\boldsymbol{u} \times \boldsymbol{v} = e_{ijk} u_j v_k \, \hat{\boldsymbol{e}}_i$

$\boldsymbol{\alpha} \times \boldsymbol{u} = e_{jkl} \alpha_{ik} u_l \, \hat{\boldsymbol{e}}_i \otimes \hat{\boldsymbol{e}}_j$

Dot and double-dot product: $\boldsymbol{\alpha} \cdot \boldsymbol{B} = \alpha_{ij} B_{jk} \, \hat{\boldsymbol{e}}_i \otimes \hat{\boldsymbol{e}}_k$

$\boldsymbol{\alpha} \cdot \boldsymbol{u} = \alpha_{ij} u_j \, \hat{\boldsymbol{e}}_i$

$\boldsymbol{v} \cdot \boldsymbol{B} = v_i B_{ij} \, \hat{\boldsymbol{e}}_j$

$\mathbf{X} : \boldsymbol{\alpha} = e_{ijk} \alpha_{jk} \hat{\boldsymbol{e}}_i$

$\mathbb{C} : \boldsymbol{\alpha} = \mathbb{C}_{ijkl} \alpha_{kl} \, \hat{\boldsymbol{e}}_i \otimes \hat{\boldsymbol{e}}_j$

Differential operators: $\nabla \boldsymbol{u} = \operatorname{grad} \boldsymbol{u} = u_{i,j} \, \hat{\boldsymbol{e}}_i \otimes \hat{\boldsymbol{e}}_j$

$\nabla \boldsymbol{\alpha} = \operatorname{grad} \boldsymbol{\alpha} = \alpha_{ij,k} \, \hat{\boldsymbol{e}}_i \otimes \hat{\boldsymbol{e}}_j \otimes \hat{\boldsymbol{e}}_k$

$\nabla \cdot \boldsymbol{u} = \operatorname{div} \boldsymbol{u} = u_{i,i}$

$\nabla \cdot \boldsymbol{\alpha} = \operatorname{div} \boldsymbol{\alpha} = \alpha_{ij,j} \, \hat{\boldsymbol{e}}_i$

$\nabla \times \boldsymbol{u} = \operatorname{curl} \boldsymbol{u} = e_{ijk} u_{k,j} \, \hat{\boldsymbol{e}}_i$

$\nabla \times \boldsymbol{\alpha} = \operatorname{curl} \boldsymbol{\alpha} = e_{jkl} \alpha_{il,k} \, \hat{\boldsymbol{e}}_i \otimes \hat{\boldsymbol{e}}_j \,,$

where the comma indicates differentiation with respect to a given coordinate. Time derivatives are indicated by a superposed dot $\dot{\square}$.

3. The TFDM model

In the following, the governing equations and the initial and boundary conditions of the TFDM model (Upadhyay (2020)) are briefly recalled, followed by a non-dimensionalization of the problem.

3.1. Field equations of TFDM

Consider a simply connected body $\Omega \subset \mathcal{E}^3$, where $\mathcal{E}^3$ is the three-dimensional Euclidean point space, whose boundary is $\partial\Omega$. A small deformation hypothesis is considered and the model is assumed to operate at the length scale where individual line defects can be distinguished. In this setting, the equation set of the TFDM model is (Upadhyay (2020)):

$$\boldsymbol{U}^p = \nabla \boldsymbol{z}^p + \boldsymbol{\chi}^p \quad \text{in} \quad \Omega \times [0, t_F] \tag{3.1a}$$
$$\boldsymbol{\alpha}^p = -\nabla \times \boldsymbol{\chi}^p \quad \text{in} \quad \Omega \times [0, t_F] \tag{3.1b}$$
$$\nabla \cdot \boldsymbol{\chi}^p = 0 \quad \text{in} \quad \Omega \times [0, t_F] \tag{3.1c}$$
$$\nabla \cdot \nabla \dot{\boldsymbol{z}}^p = \nabla \cdot (\boldsymbol{\alpha}^p \times \boldsymbol{v}) \quad \text{in} \quad \Omega \times (0, t_F] \tag{3.1d}$$
$$\dot{\boldsymbol{U}}^p = \boldsymbol{\alpha}^p \times \boldsymbol{v} \quad \text{in} \quad \Omega \times [0, t_F] \tag{3.1e}$$
$$\dot{\boldsymbol{\alpha}}^p = -\nabla \times (\boldsymbol{\alpha}^p \times \boldsymbol{v}) \quad \text{in} \quad \Omega \times (0, t_F] \tag{3.1f}$$
$$\boldsymbol{v} = \frac{1}{B}\boldsymbol{f} \quad \text{in} \quad \Omega \times [0, t_F] \tag{3.1g}$$

$$\nabla \cdot \boldsymbol{\sigma} = 0 \quad \text{in} \quad \Omega \times [0, t_F] \tag{3.1h}$$
$$\boldsymbol{\sigma} = \mathbb{C} : (\nabla \boldsymbol{u} - \boldsymbol{U}^p) - \boldsymbol{\beta}\Delta\theta \quad \text{in} \quad \Omega \times [0, t_F] \tag{3.1i}$$

$$\rho c_\varepsilon \dot{\theta} = -\nabla \cdot \boldsymbol{q} + \boldsymbol{\sigma} : \dot{\boldsymbol{U}}^p - \theta\boldsymbol{\beta} : (\nabla \dot{\boldsymbol{u}} - \dot{\boldsymbol{U}}^p) + \rho r \quad \text{in} \quad \Omega \times (0, t_F] \tag{3.1j}$$
$$\boldsymbol{q} = -\boldsymbol{K} \cdot \nabla\theta \quad \text{in} \quad \Omega \times [0, t_F], \tag{3.1k}$$

where t_F is the total simulation time. The first set of Equations 3.1a to 3.1g are the kinematic equations of the model. The Stokes-Helmholtz decomposition is used in Eq. 3.1a to uniquely decompose the plastic distortion tensor $\boldsymbol{U}^p$ into the sum of a compatible ($\nabla \boldsymbol{z}^p$, curl-free) and an incompatible ($\boldsymbol{\chi}^p$, divergence-free) part (Acharya & Roy (2006)). Eq. 3.1b expresses the plastic incompatibility due to the presence of dislocations through a geometry statement. Together with Eq. 3.1c, these equations allow for the unique determination of $\boldsymbol{\chi}^p$ given the polar dislocation density tensor $\boldsymbol{\alpha}^p$, and ensure that $\boldsymbol{\chi}^p = 0$ whenever $\boldsymbol{\alpha}^p = 0$. Eq. 3.1g is a constitutive relationship for the dislocation velocity field $\boldsymbol{v}$ as a function of its driving force $\boldsymbol{f} = (\boldsymbol{\sigma} \cdot \boldsymbol{\alpha}^p) : \mathbf{X}$, where $\boldsymbol{\sigma}$ is the Cauchy stress tensor, and $1/B$ is the dislocation mobility coefficient. In the case of a single dislocation, $\boldsymbol{f}$ reduces to the Peach-Koehler force exerted on a dislocation line (Peach & Koehler (1950)). Eq. 3.1d gives the evolution of the compatible part of the plastic distortion tensor, which stores the information of the plastic deformation history from the start of the simulation. Eq. 3.1e accounts for the plastic slip distortion in the body due to dislocation motion. Eq. 3.1f arises from the conservation of Burgers vector in the body (see Acharya (2011)). It represents the transport of dislocation lines and naturally accounts for dislocation annihilation. The conservation of the Burgers vector results in the Nye's tensor $\boldsymbol{\alpha} = \boldsymbol{\alpha}^p + \boldsymbol{\alpha}^\theta$ (Upadhyay (2020)). In this relation, $\boldsymbol{\alpha}^\theta$ is the thermal defect density tensor, which arises due to incompatibilities in the thermal strain field ($\boldsymbol{\varepsilon}^\theta := \boldsymbol{\gamma}\Delta\theta$), and is defined as $\boldsymbol{\alpha}^\theta := -\nabla \times (\boldsymbol{\gamma}\Delta\theta)$, where $\boldsymbol{\gamma}$ is the positive-definite thermal expansion tensor (considered isotropic in this work i.e., $\boldsymbol{\gamma} = \gamma\mathbb{1}$) and $\Delta\theta = \theta - \theta_0$ is the temperature field deviation from a reference temperature θ_0. The outcomes of this decomposition of Nye's tensor are not explored in the present work.

The governing equation Eq. 3.1h is the static mechanical equilibrium equation neglecting body forces. Eq. 3.1i is the Neumann-Duhamel's constitutive equation for $\boldsymbol{\sigma}$ in thermoelasticity, which reduces to the 3D Hooke's law under isothermal condition at θ_0. $\mathbb{C}$ is the fourth-order stiffness tensor, which, considering isotropic elasticity, is expressed as $\mathbb{C}_{ijkl} = \lambda\delta_{ij}\delta_{kl} + \mu(\delta_{ik}\delta_{jl} + \delta_{il}\delta_{jk})$, where λ and μ are the first and second Lamé parameters, respectively; note that the model and its numerical implementation are capable of handling anisotropic elasticity without any changes to the implementation. $\boldsymbol{u}$ is the total displacement vector, and $\boldsymbol{\beta} = \mathbb{C} : \boldsymbol{\gamma}$ is the second-order thermal moduli tensor.

Finally, the conservation of energy expressed by the first law of thermodynamics gives rise to the temperature evolution governing Eq. 3.1j. It is coupled with dislocation activity and elasticity through the second and third terms on the right-hand side, respectively. ρ is the material density, c_ε is the specific heat capacity at constant strain, $\boldsymbol{q}$ is the heat flux vector, and r is an internal heat source term. The heat flux $\boldsymbol{q}$ is constitutively specified through the generalized Fourier's law in Eq. 3.1k, where $\boldsymbol{K}$ is the second order thermal conductivity tensor. All the material properties are temperature-dependent.

Note that the constitutive relations of the TFDM model are deduced from material frame indifference and the requirement that the global dissipation rate D is non-negative, where D is expressed as

$$D = \int_\Omega \boldsymbol{\sigma} : \dot{\boldsymbol{U}}^p \, dV - \int_\Omega \frac{1}{\theta}(\boldsymbol{q} \cdot \nabla\theta) \, dV \geq 0 \tag{3.2}$$

3.2. Boundary and initial conditions

The theory is closed with the prescription of initial and boundary conditions (BCs) for the fields in Eq. 3.1. The BCs are given as follows:

$$\begin{aligned}
\boldsymbol{\chi}^p \cdot \hat{\boldsymbol{n}} &= 0 \quad \text{on} \quad \partial\Omega \times [0, t_F] && \text{(3.3a)}\\
(\nabla \dot{\boldsymbol{z}}^p - \boldsymbol{\alpha}^p \times \boldsymbol{v}) \cdot \hat{\boldsymbol{n}} &= 0 \quad \text{on} \quad \partial\Omega \times (0, t_F] && \text{(3.3b)}\\
(\boldsymbol{v} \cdot \hat{\boldsymbol{n}})\, \boldsymbol{\alpha}^p &= 0 \quad \text{on} \quad \partial\Omega \times (0, t_F] && \text{(3.3c)}\\
\hline
\boldsymbol{u} &= \bar{\boldsymbol{u}} \quad \text{on} \quad \partial\Omega^u \times [0, t_F] && \text{(3.3d)}\\
\boldsymbol{\sigma} \cdot \hat{\boldsymbol{n}} &= \bar{\boldsymbol{t}} \quad \text{on} \quad \partial\Omega^t \times [0, t_F] && \text{(3.3e)}\\
\hline
\theta &= \bar{\theta} \quad \text{on} \quad \partial\Omega^\theta \times [0, t_F] && \text{(3.3f)}\\
\boldsymbol{q} \cdot \hat{\boldsymbol{n}} &= \bar{q} \quad \text{on} \quad \partial\Omega^q \times [0, t_F], && \text{(3.3g)}
\end{aligned}$$

where $\partial\Omega^u \cup \partial\Omega^t = \partial\Omega$, $\partial\Omega^u \cap \partial\Omega^t = \emptyset$, $\partial\Omega^\theta \cup \partial\Omega^q = \partial\Omega$ and $\partial\Omega^\theta \cap \partial\Omega^q = \emptyset$. The overbars in Equations 3.3d to 3.3g indicate prescribed values. Equations 3.3a and 3.3b allow for the unique determination of the plastic distortion tensor $\boldsymbol{U}^p$ given $\boldsymbol{\alpha}^p$ and $\boldsymbol{v}$. Note that from Eq. 3.1d, only $\nabla \boldsymbol{z}^p$ (and not $\boldsymbol{z}^p$) is required here to obtain a unique $\boldsymbol{U}^p$. Thus, $\dot{\boldsymbol{z}}^p$ is arbitrarily specified at one point of the body, without loss of generality. Eq. 3.3c implies that dislocations are not allowed to enter or leave the body through the boundaries. Equations 3.3d and 3.3e are the displacement and traction BCs for the static mechanical equilibrium Eq. 3.1h, and Eqs. 3.3f and 3.3g correspond to the imposed temperature field and heat flux on the boundary, required to solve the temperature evolution Eq. 3.1j.

The initial ($t = 0$) conditions are

$$\begin{aligned}
\boldsymbol{z}^p(\bullet, 0) &= 0 \quad \text{in} \quad \Omega && \text{(3.4a)}\\
\boldsymbol{\alpha}^p(\bullet, 0) &= \boldsymbol{\alpha}^p_0(\bullet) \quad \text{in} \quad \Omega && \text{(3.4b)}\\
\theta(\bullet, 0) &= \theta_0(\bullet) \quad \text{in} \quad \Omega\,, && \text{(3.4c)}
\end{aligned}$$

where $\boldsymbol{\alpha}^p_0$ and θ_0 are prescribed values.

3.3. Nondimensionalization

Similar to Zhang et al. (2015), the following dimensionless variables are introduced:

$$\begin{gathered}
\tilde{\theta} = \frac{\theta}{\theta_0}\,; \quad \tilde{t} = \frac{v_s}{l_c} t\,; \quad \tilde{\boldsymbol{x}} = \frac{1}{l_c}\boldsymbol{x}\,; \quad \tilde{\boldsymbol{\sigma}}^{eq} = \frac{1}{\mu}\boldsymbol{\sigma}\,; \quad \tilde{\boldsymbol{v}} = \frac{1}{v_s}\boldsymbol{v}\,; \quad \tilde{\boldsymbol{\alpha}}^p = l_c \boldsymbol{\alpha}^p; \quad \dot{\tilde{\boldsymbol{U}}}^p = \tilde{\boldsymbol{\alpha}}^p \times \tilde{\boldsymbol{v}}\\
\tilde{\boldsymbol{u}} = \frac{1}{l_c}\boldsymbol{u}\,; \quad \tilde{\boldsymbol{K}} = \frac{1}{\rho c_\varepsilon v_s l_c}\boldsymbol{K}\,; \quad \tilde{\boldsymbol{\sigma}}^{th} = \frac{1}{\rho c_\varepsilon \theta_0}\boldsymbol{\sigma}\,; \quad \tilde{\boldsymbol{\beta}} = \frac{1}{\rho c_\varepsilon}\boldsymbol{\beta}\,; \quad \tilde{r} = \frac{l_c}{v_s c_\varepsilon \theta_0} r,
\end{gathered} \tag{3.5}$$

where v_s is the shear wave propagation speed, l_c is a characteristic length of the problem (e.g., the Burgers vector magnitude), μ is computed for a given Young's modulus E and Poisson ratio ν, and $\boldsymbol{\sigma}^{eq}$ and $\boldsymbol{\sigma}^{th}$ are the dimensionless stress tensors considered when solving Equations 3.1h and 3.1j, respectively. The governing equations in Eq. 3.1 can thus be written in a dimensionless form as

$$\begin{aligned}
\tilde{\nabla} \cdot \tilde{\boldsymbol{\sigma}}^{eq} &= 0 && \text{in} \quad \tilde{\Omega} \times [0, \tilde{t}_F] && \text{(3.6a)}\\
\dot{\tilde{\theta}} &= \tilde{\nabla} \cdot (\tilde{\boldsymbol{K}} \cdot \tilde{\nabla}\tilde{\theta}) + \tilde{\boldsymbol{\sigma}}^{th} : \dot{\tilde{\boldsymbol{U}}}^p - \tilde{\theta}\tilde{\boldsymbol{\beta}} : (\tilde{\nabla}\dot{\tilde{\boldsymbol{u}}} - \dot{\tilde{\boldsymbol{U}}}^p) + \tilde{r} && \text{in} \quad \tilde{\Omega} \times (0, \tilde{t}_F] && \text{(3.6b)}\\
\dot{\tilde{\boldsymbol{\alpha}}}^p &= -\tilde{\nabla} \times (\tilde{\boldsymbol{\alpha}}^p \times \tilde{\boldsymbol{v}}) && \text{in} \quad \tilde{\Omega} \times (0, \tilde{t}_F]\,, && \text{(3.6c)}
\end{aligned}$$

where the superposed dot indicates time derivative with respect to $\tilde{t}$, $\tilde{\Omega}$ is the nondimensional domain, and $\tilde{t}_F = \frac{v_s}{l_c} t_F$.

Henceforth, all the variables are considered in their dimensionless form. The superposed tilde is dropped for convenience unless the distinction between dimensional and dimensionless variables is explicitly made.

4. Finite element formulation and algorithm

In this section, the approximation of the TFDM model using the FEM is presented. The variational forms of the governing equations in Eq. 3.6 and plastic distortion in Equations 3.1b to 3.1d are introduced, and the algorithm is presented at the end.

4.1. Evolution of $\boldsymbol{\alpha}^p$

The dislocation density transport, Eq. 3.1f, is solved using a time-explicit Runge-Kutta Discontinuous Galerkin (RKDG) scheme, which was proposed in Upadhyay & Bleyer (2021).

Consider the discretization of Ω into a mesh Ω_h, whose boundary is $\partial\Omega_h$. Henceforth, the subscript h indicates the projection of a given variable onto the mesh Ω_h i.e., $\boldsymbol{\alpha}_h^p := \Pi\boldsymbol{\alpha}^p$, where Π is the projection operator. Consider the tensor function space $\mathcal{V}_h^\alpha = \{\boldsymbol{\eta} \in [\mathcal{P}_D^1(\Omega_h)]^{3\times3}\}$, where $\mathcal{P}_D^1$ denotes the space of piecewise continuous linear polynomials defined over Ω_h and the superscript 3 corresponds to the space dimension. The variational formulation for the space discretization of Eq. 3.1f reads (Upadhyay & Bleyer (2021)): for all test functions $\boldsymbol{\delta\alpha}_h \in \mathcal{V}_h^\alpha$, find $\boldsymbol{\alpha}_h^p \in \mathcal{V}_h^\alpha$ such that

$$\int_{\Omega_h} \dot{\boldsymbol{\alpha}}_h^p : \boldsymbol{\delta\alpha}_h \, dV + a_h^{upw}(\boldsymbol{\alpha}_h^p, \boldsymbol{\delta\alpha}_h) \, dV = 0, \quad \forall t \in (0, t_F], \tag{4.1}$$

where $a_h^{upw}(\boldsymbol{\alpha}_h^p, \boldsymbol{\delta\alpha}_h)$ is the upwind DG bilinear form, defined as:

$$\begin{aligned} a_h^{upw}(\boldsymbol{\alpha}_h^p, \boldsymbol{\delta\alpha}_h) := &\int_{\Omega_h} (\boldsymbol{\alpha}_h^p \cdot \boldsymbol{\mu}) : \boldsymbol{\delta\alpha}_h \, dV + \int_{\Omega_h} [(\nabla_h \boldsymbol{\alpha}_h^p) \cdot \boldsymbol{v} - (\nabla_h \cdot \boldsymbol{\alpha}_h^p) \otimes \boldsymbol{v}] : \boldsymbol{\delta\alpha}_h \, dV \\ &+ \int_{\partial\Omega_h} (\boldsymbol{v} \cdot \hat{\boldsymbol{n}})^{\ominus} \boldsymbol{\alpha}_h^p : \boldsymbol{\delta\alpha}_h \, dS - \sum_{F \in \mathcal{F}_h^i} \int_F (\boldsymbol{v} \cdot \hat{\boldsymbol{n}}_F) [\![\boldsymbol{\alpha}_h^p]\!] : \{\!\{\boldsymbol{\delta\alpha}_h\}\!\} \, dS \\ &+ \sum_{F \in \mathcal{F}_h^i} \int_F \frac{C_\alpha}{2} |\boldsymbol{v} \cdot \hat{\boldsymbol{n}}_F| [\![\boldsymbol{\alpha}_h^p]\!] : [\![\boldsymbol{\delta\alpha}_h]\!] \, dS, \end{aligned} \tag{4.2}$$

where $\boldsymbol{\mu} := (\nabla \cdot \boldsymbol{v})\,\mathbb{1} - (\nabla \boldsymbol{v})^T$ and $C_\alpha \geq 0$ is a user-specified parameter that penalizes the jumps in the trial and test functions across mesh interfaces. A parametric study conducted in Upadhyay & Bleyer (2021) concluded that for Eq. 4.2, the optimal value for the penalty factor is $C_\alpha = 1$, which is the value adopted in this work. ∇_h denotes the broken gradient operator, which is the gradient defined within each element of the mesh, but not at the interfaces between elements. $\mathcal{F}_h^i$ denotes the collection of the interfaces in the mesh and $\hat{\boldsymbol{n}}_F$ are interface normals. $x^{\ominus} := \frac{1}{2}(|x| - x)$ denotes the negative part of a real number x. The operators $\{\!\{\boldsymbol{\eta}\}\!\}$ and $[\![\boldsymbol{\eta}]\!]$ represent the average and the jump, respectively, of a second-order tensor $\boldsymbol{\eta}$, acting individually on each component of $\boldsymbol{\eta}$. Note that the dislocation velocity vector $\boldsymbol{v}$ is assumed to be dependent on $\boldsymbol{\alpha}^p$ of the previous time step, which allows treating Eq. 4.1 as linear on $\boldsymbol{\alpha}^p$.

The time discretization of Eq. 4.1 is performed using a time-explicit strong stability preserving (SSP) RK scheme. A superscript between parenthesis (n) indicates the value of a variable at time t^n, and the superscript $(n+1)$ at time $t + \Delta t$, where Δt is a constant time-step. The s-stage RK scheme for the dislocation transport is written as (Upadhyay & Bleyer (2021))

$$\begin{aligned} \boldsymbol{\alpha}_h^{p(n,0)} &= \boldsymbol{\alpha}_h^{p(n)} \\ \int_{\Omega_h} \boldsymbol{\alpha}_h^{p(n,i)} : \boldsymbol{\delta\alpha}_h \, dV &= \sum_{j=0}^{i-1} \left(\int_{\Omega_h} d^{ij} \boldsymbol{\alpha}_h^{p(n,j)} : \boldsymbol{\delta\alpha}_h \, dV - \Delta t \, g^{ij} a_h^{upw}(\boldsymbol{\alpha}_h^{p(n,j)}, \boldsymbol{\delta\alpha}_h) \right) \\ \boldsymbol{\alpha}_h^{p(n+1)} &= \boldsymbol{\alpha}_h^{p(n,s)}, \end{aligned} \tag{4.3}$$

where $[d^{ij}]_{1\leq i\leq s, 0\leq j\leq i-1}$ and $[g^{ij}]_{1\leq i\leq s, 0\leq j\leq i-1}$ are lower triangular matrices. In this work, 2-stage and 3-stage SSPRK schemes are used. The matrices for SSPRK2 are:

$$d = \begin{bmatrix} 1 & \\ 1/2 & 1/2 \end{bmatrix}, \quad g = \begin{bmatrix} 1 & \\ 0 & 1/2 \end{bmatrix}$$

For SSPRK3, the following matrices are used:

$$d = \begin{bmatrix} 1 & & \\ 1/2 & 1/2 & \\ 1/3 & 1/3 & 1/3 \end{bmatrix}, \quad g = \begin{bmatrix} 1 & & \\ 0 & 1/2 & \\ 0 & 0 & 1/3 \end{bmatrix}$$

4.2. Computation of $\boldsymbol{\chi}^p$

Following Roy & Acharya (2005), $\boldsymbol{\chi}^p$ is computed using the LSFEM. The tensor function space considered is $\mathcal{V}_h^{\chi} = \{\boldsymbol{\eta} \in [\mathcal{P}^1(\Omega_h)]^{3\times 3}\}$, where $\mathcal{P}^1$ denotes the space of linear continuous polynomials in Ω_h. The variational form of Equations 3.1b and 3.1c is written as: for all $\boldsymbol{\delta\chi}_h \in \mathcal{V}_h^{\chi}$, find $\boldsymbol{\chi}_h^p \in \mathcal{V}_h^{\chi}$ such that

$$\int_{\Omega_h} (\nabla\times\boldsymbol{\chi}_h^p) : (\nabla\times\boldsymbol{\delta\chi}_h)\, dV + \int_{\Omega_h} (\nabla\cdot\boldsymbol{\chi}_h^p)\cdot(\nabla\cdot\boldsymbol{\delta\chi}_h)\, dV + \frac{C_{\chi}}{h}\int_{\partial\Omega_h} (\boldsymbol{\chi}_h^p\cdot\boldsymbol{n})\cdot(\boldsymbol{\delta\chi}_h\cdot\boldsymbol{n})\, dS = -\int_{\Omega_h} \boldsymbol{\alpha}_h^p : (\nabla\times\boldsymbol{\delta\chi}_h)\, dV \quad (4.4)$$

In Eq. 4.4, the third term on the left-hand side weakly enforces the boundary condition 3.3a. C_{χ} is a penalty factor and h is a mesh size parameter. Numerical tests show that, while increasing C_{χ} increases the accuracy of the approximation of Eq. 3.3a, it also considerably increases computational cost due to the bad conditioning of the system matrix corresponding to the assembly of the bilinear form (left-hand side) of Eq. 4.4. In the current implementation, $C_{\chi} = 100$ is found to be an adequate compromise for the aforementioned problem.

4.3. Evolution of $\boldsymbol{z}^p$

A continuous Galerkin space discretization and a forward Euler time discretization are used to update $\boldsymbol{z}^p$. Consider the vector function space $\mathcal{V}_h^z = \{\boldsymbol{\eta} \in [\mathcal{P}^2(\Omega_h)]^3 \,|\, \boldsymbol{\eta}(0,\bullet) = 0\}$, where $\mathcal{P}^2$ corresponds to the space of continuous quadratic polynomials in Ω_h. Then, for each time step t^{n+1}, the variational form of Eq. 3.1d is written as: for all $\boldsymbol{\delta z}_h \in \mathcal{V}_h^z$, find $\boldsymbol{z}_h^{p(n+1)} \in \mathcal{V}_h^z$ such that

$$\int_{\Omega} \nabla\boldsymbol{z}_h^{p(n+1)} : \nabla\boldsymbol{\delta z}_h\, dV = \Delta t \int_{\Omega} (\boldsymbol{\alpha}_h^{p(n)}\times\boldsymbol{v}^{(n)}) : \nabla\boldsymbol{\delta z}_h\, dV + \int_{\Omega} \nabla\boldsymbol{z}_h^{p(n)} : \nabla\boldsymbol{\delta z}_h\, dV, \quad (4.5)$$

with $\dot{\boldsymbol{z}}_h^p(0,\bullet) = 0$ being taken into account in the definition of $\mathcal{V}_h^z$ (also see argument after Eq. 3.3b).

4.4. Computation of $\boldsymbol{u}$

The static equilibrium equation Eq. 3.6a is solved to obtain $\boldsymbol{u}$ using a continuous Galerkin approach. Consider the vector function spaces $\mathcal{V}_h^u = \{\boldsymbol{\eta} \in [\mathcal{P}^2(\Omega_h)]^3 \,|\, \boldsymbol{\eta} = \bar{\boldsymbol{u}} \text{ on } \partial\Omega_u\}$ and $\mathcal{V}_{h,0}^u = \{\boldsymbol{\eta} \in [\mathcal{P}^2(\Omega_h)]^3 \,|\, \boldsymbol{\eta} = 0 \text{ on } \partial\Omega_u\}$. The variational formulation of Eq. 3.6a is written as: for all $\boldsymbol{\delta u}_h \in \mathcal{V}_{h,0}^u$, find $\boldsymbol{u}_h \in \mathcal{V}_h^u$ such that

$$\int_{\Omega} \left(\mathbb{C} : \nabla\boldsymbol{u}_h\right) : \nabla\boldsymbol{\delta u}_h\, dV = \int_{\partial\Omega^t} \bar{\boldsymbol{t}}\cdot\boldsymbol{\delta u}_h\, dS + \int_{\Omega} \left\{[\mathbb{C} : (\nabla\boldsymbol{z}_h^p + \boldsymbol{\chi}_h^p)] + \boldsymbol{\beta}\Delta\theta_h\right\} : \nabla\boldsymbol{\delta u}_h\, dV \quad (4.6)$$

4.5. Evolution of θ

The temperature evolution Eq. 3.6b is solved using a semi-implicit scheme in time, and a continuous Galerkin discretization in space. Consider the finite-dimensional function spaces $\mathcal{V}_h^{\theta} = \{\eta \in \mathcal{P}^2(\Omega_h) \,|\, \eta = \bar{\theta} \text{ on } \partial\Omega_{\theta}\}$ and $\mathcal{V}_{h,0}^{\theta} = \{\eta \in \mathcal{P}^2(\Omega_h) \,|\, \eta = 0 \text{ on } \partial\Omega_{\theta}\}$. The variational formulation of the temperature evolution reads: for all $\delta\theta \in \mathcal{V}_{h,0}^{\theta}$, find $\theta_h \in \mathcal{V}_h^{\theta}$ such that

$$\begin{aligned}\frac{1}{\Delta t}\int_{\Omega} \left(\theta_h^{(n+1)} - \theta_h^{(n)}\right)\delta\theta\, dV + \int_{\Omega} \left[\boldsymbol{K}\cdot\nabla\theta_h^{(n+1)}\right]\cdot\nabla(\delta\theta)\, dV + \int_{\Omega} \theta^{(n+1)}\,\boldsymbol{\beta} : \left(\nabla\dot{\boldsymbol{u}}_h^{(n)} - \dot{\boldsymbol{U}}_h^{p(n)}\right)\delta\theta\, dV \\ = -\int_{\partial\Omega^q} \bar{q}\,\delta\theta\, dS + \int_{\Omega} \left(\boldsymbol{\sigma}_h^{th(n)} : \dot{\boldsymbol{U}}_h^{p(n)}\right)\delta\theta\, dV + \int_{\Omega} r^{(n)}\delta\theta\, dV\end{aligned} \quad (4.7)$$

The scheme is semi-implicit in time because $\boldsymbol{\sigma}_h^{th(n)}$, $\nabla\dot{\boldsymbol{u}}_h^{(n)}$ and $\dot{\boldsymbol{U}}_h^{p(n)}$ are dependent on θ but they enter as known data in this equation.

4.6. Small-strains TFDM-FE algorithm

The variational Eqs. 4.3 to 4.7 are implemented using the Python front-end of the FEniCS library (Logg et al. (2012)), which is an open-source PDE solver via the FEM. The implemented algorithm is shown in Algorithm 1. A staggered approach is used to solve Eqs. 4.3 to 4.7.

Algorithm 1: Quasi-static, small deformation TFDM-FE algorithm

Data: FE mesh, and simulation and material parameters
Result: $\boldsymbol{\alpha}^p$, $\boldsymbol{\chi}^p$, $\boldsymbol{z}^p$, $\boldsymbol{u}$, θ

begin
  assign $\boldsymbol{\alpha}_0^p$, θ_0, $\boldsymbol{z}_0^p = 0$, $\bar{\boldsymbol{t}}$, $\bar{\boldsymbol{u}}$, $\bar{q}$, $\bar{\theta}$, Δt, t_F
  $\boldsymbol{\chi}_0^p \longleftarrow$ solve Eq. 4.4
  $\boldsymbol{u}_0 \longleftarrow$ solve Eq. 4.6
  $\boldsymbol{\sigma}_0 \longleftarrow \mathbb{C} : (\nabla \boldsymbol{u}_0 - \boldsymbol{\chi}_0^p)$
  $\boldsymbol{v}_0 \longleftarrow f(\boldsymbol{\sigma}_0, \boldsymbol{\alpha}_0^p)$
  while $t < t_F$ **do**
    $\boldsymbol{\alpha}^{p(n+1)} \longleftarrow$ solve Eq. 4.3
    $\boldsymbol{\chi}^{p(n+1)} \longleftarrow$ solve Eq. 4.4
    $\boldsymbol{z}^{p(n+1)} \longleftarrow$ solve Eq. 4.5
    $\boldsymbol{u}^{(n+1)} \longleftarrow$ solve Eq. 4.6
    $\boldsymbol{\sigma}^{(n+1)} \longleftarrow \mathbb{C} : \left(\nabla(\boldsymbol{u}^{(n+1)} - \boldsymbol{z}^{p(n+1)}) - \boldsymbol{\chi}^{p(n+1)}\right) - \boldsymbol{\beta}\Delta\theta^{(n)}$
    $\nabla \dot{\boldsymbol{u}}^{(n+1)} \longleftarrow \frac{1}{\Delta t}\left(\nabla \boldsymbol{u}^{(n+1)} - \nabla \boldsymbol{u}^{(n)}\right)$
    $\dot{\boldsymbol{U}}^{p(n+1)} \longleftarrow \boldsymbol{\alpha}^{p(n+1)} \times \boldsymbol{v}^{(n)}$
    $\theta^{(n+1)} \longleftarrow$ solve Eq. 4.7
    $\boldsymbol{v}^{(n+1)} \longleftarrow f\left(\boldsymbol{\sigma}^{(n+1)}, \boldsymbol{\alpha}^{p(n+1)}\right)$
    update temperature-dependent material parameters
    $t \longleftarrow t + \Delta t$
  end

5. Results and discussion

5.1. Temperature evolution due to dislocation motion: comparison between TFDM-FE and analytical solution

A comparison is performed between the analytical solution of the temperature field generated due to the motion of a dislocation, derived in Gurrutxaga-Lerma (2017), and the temperature field computed through Eq. 4.7, to validate the dislocation activity-temperature evolution coupling of the TFDM model. The analytical expression was obtained by solving the two-dimensional heat equation uncoupled from elasticity and considering that the dislocation acts as a singular (point) heat source according to $q_d = b\tau v\,\delta(x - vt)\delta(y)$. In this expression, q_d is the heat generated by the moving dislocation, b is the magnitude of the Burgers vector, τ is the resolved shear stress applied on the dislocation, v is the dislocation glide speed, and the delta functions account for the motion of the dislocation on the $y = 0$ plane. The resolved shear stress τ is related to v through the mobility law (Gurrutxaga-Lerma (2017))

$$\tau = \frac{d_0 v}{b}\frac{1}{1 - \frac{v^2}{v_s^2}}, \tag{5.1}$$

where d_0 is the low-speed drag coefficient, and v_s is the shear wave propagation velocity in the material. The main requirement for the adoption of this relation is that, for low speeds, the slope of $\tau(v)$ agrees with the observed linear viscous drag coefficient, and that it saturates as v approaches v_s. In Gurrutxaga-Lerma (2017), a constant v, and consequently, a constant τ are assumed. The body is assumed to be initially at a homogeneous temperature θ_0. The resulting analytical expression for the temperature difference profile $\Delta\theta$ at a given time t in the bulk of a body reads

$$\Delta\theta(x, y, t) = \frac{1}{4\pi K}\frac{v^2 d_0}{1 - \frac{v^2}{v_s^2}}\int_0^t \frac{exp\left(-\frac{(x - x_c - vt')^2 + (y - y_c)^2}{4\kappa_v(t - t')}\right)}{t - t'}\,dt', \tag{5.2}$$

where K is the magnitude of thermal conductivity, κ_v is the thermal diffusivity at constant deformation, and (x_c, y_c) denotes the initial position of the dislocation.

Eq. 5.2 is numerically implemented using a C++ algorithm, considering a (1×1) μm^2 domain, discretized by a regular 5000×5000 grid. The integral term is computed by a composite Simpson rule, with the time interval divided into 1000 steps. The values of the coefficients considered in Eq. 5.2 are shown in Tab. 1.

The TFDM-FE simulation is conducted on a $(1 \times 1 \times 1000)$ μm^3 domain in the (x, y, z) directions, respectively. An edge dislocation whose Burgers and line vectors are parallel to $\hat{\mathbf{e}}_1$ and $\hat{\mathbf{e}}_3$, respectively, is embedded at the centre of the domain such that $\boldsymbol{\alpha}^p = \alpha^p_{13} \hat{\mathbf{e}}_1 \otimes \hat{\mathbf{e}}_3$. The initial dislocation density is assumed to be

$$\alpha^{p(0)}_{13} = \phi_0 \, exp\left(-\frac{(x - x_c)^2 + (y - y_c)^2}{2r_c^2} \right), \tag{5.3}$$

corresponding to a Gaussian profile. In this expression, ϕ_0 is a parameter that controls the magnitude of the dislocation density, x_c and y_c represent the initial position of the centre of the dislocation core, and r_c controls the dislocation core spread. To simulate a single dislocation in the model, ϕ_0 must be set such that $\int_S \phi_0 \, dS = b$, where S is an arbitrary open surface whose bounding curve encloses the dislocation line, and whose normal is, in this case, parallel to the $\hat{\mathbf{e}}_3$ direction. Usually, a different value of ϕ_0 is required for different meshes to ensure the previously mentioned surface integral. The dislocation is assumed to be moving with a constant speed $v_0 > 0$ along the x-direction, such that $\boldsymbol{v} = v_0 \, \hat{\mathbf{e}}_1$.

The domain is considerably elongated in the z direction and discretized by a single element. This is done to approximate the simulation to a 2D setting using the native 3D FE implementation of the TFDM model. The (x, y) planes are discretized by a mesh that is structured and fine on the region where dislocation motion occurs, and unstructured and coarse elsewhere, as seen in Fig. S1.

Table 1: Material parameters for Al and other coefficients used in Eq. 5.2 and in the FE simulations

K (W/(m K))	d_0 (Pa · s)	v_s (m/s)	x_c (μm)	y_c (μm)	κ_v (m^2/s)	γ (K^{-1})
205	2×10^{-5}	2980	0.5	0.5	9.7×10^{-5}	2.2×10^{-5}

E (GPa)	ν (-)	ρ (kg/m^3)	l_c (nm)	θ_0 (K)	c_ϵ (J/(kg K))	b (nm)
63.2	0.32	2700	1	298	782.74	0.286

For the dislocation density evolution, Eq. 4.3 is solved using the SSPRK3 scheme. Concerning the temperature evolution, since the coupling with elasticity was ignored in the derivation of the analytical solution Eq. 5.2, the third term on the left-hand side of Eq. 4.7 is neglected in the FE simulations, and the equilibrium equation Eq. 4.6 is not solved. Furthermore, a constant and homogeneous stress tensor $\boldsymbol{\sigma} = \tau \, (\hat{\mathbf{e}}_1 \otimes \hat{\mathbf{e}}_2 + \hat{\mathbf{e}}_2 \otimes \hat{\mathbf{e}}_1)$ is assigned, with τ given by Eq. 5.1. The boundary conditions assumed for the temperature evolution are $\theta = \theta_0$ on the planes $x = \{0, 1\}$ and $y = \{0, 1\}$, and zero heat flux on the planes $z = \{0, 1000\}$, with θ_0 given in Table 1. The initial setting is $\theta = \theta_0$ everywhere in Ω.

The temperature profiles predicted by the analytical solution (Eq. 5.2) and the TFDM-FE simulation are compared for three dislocation velocities, $v_0 = \{0.01, 0.5, 0.99\} v_s$, at $t = 1.02 \times 10^{-10}$ s. To facilitate the comparison, the analytical temperature profile is interpolated onto the FE mesh.

A mesh convergence analysis is performed to verify the influence of the FE discretization on the temperature profile. The element sizes used in the structured region of the mesh are $h = \{0.5, 1, 2\}$ nm. The corresponding values of ϕ_0 and r_c for the initial dislocation density Eq. 5.3 are $\phi_0 = \{1.1269 \times 10^{-2}, 2.8279 \times 10^{-3}, 7.0112 \times 10^{-4}\}$ and $r_c = \{2, 4, 8\}$ nm. This analysis is performed for $v = 0.99 \, v_s$, since this is the case for which the highest temperature change is calculated. The usual Courant-Friedrichs-Lewy (CFL) condition imposes the following constraint on the time step of the time-explicit RKDG scheme

$$\Delta t \leq \eta \, \frac{h}{v}, \tag{5.4}$$

where $\eta = 0.5$ is a user-defined parameter. Considering $h = 0.5$ and $v = 0.99$, $\Delta \tilde{t}_{CFL} = 2.5 \times 10^{-1}$. The time step chosen is $\Delta \tilde{t} = 10^{-2}$, which corresponds to $\Delta t = 3.36 \times 10^{-15}$ s, taking into account the relations in Eq. 3.5 and the values in Table 1.

The resulting temperature profiles at $t = 1.02 \times 10^{-10}$ s for $v = 0.99 \, v_s$ are presented in Fig. 1a and b. The line plot in Fig. 1c shows that the temperature profiles match almost exactly outside the dislocation core region. For the $h = 2$ mesh, the mean deviation outside the core is 0.71% and the maximum deviation is 3.67% of the FE solution with respect to the analytical one. As expected, the former converges to the latter when the element size is decreased, i.e. for $h = 0.5$, the mean deviation is 0.067% and the maximum deviation is 0.36%. At the location of the dislocation core, the FE simulation does not match the analytical result. This difference is due to the dislocation core being considered as singular in the analytical solution Eq. 5.2 whereas it is spread over a finite region in the FE simulation Eq. 5.3.

The same simulations are performed for $h = 1$ and $v = \{0.01, 0.50\} v_s$, and a similar behaviour is observed i.e., the temperature profiles computed by the two approaches match outside the dislocation core.

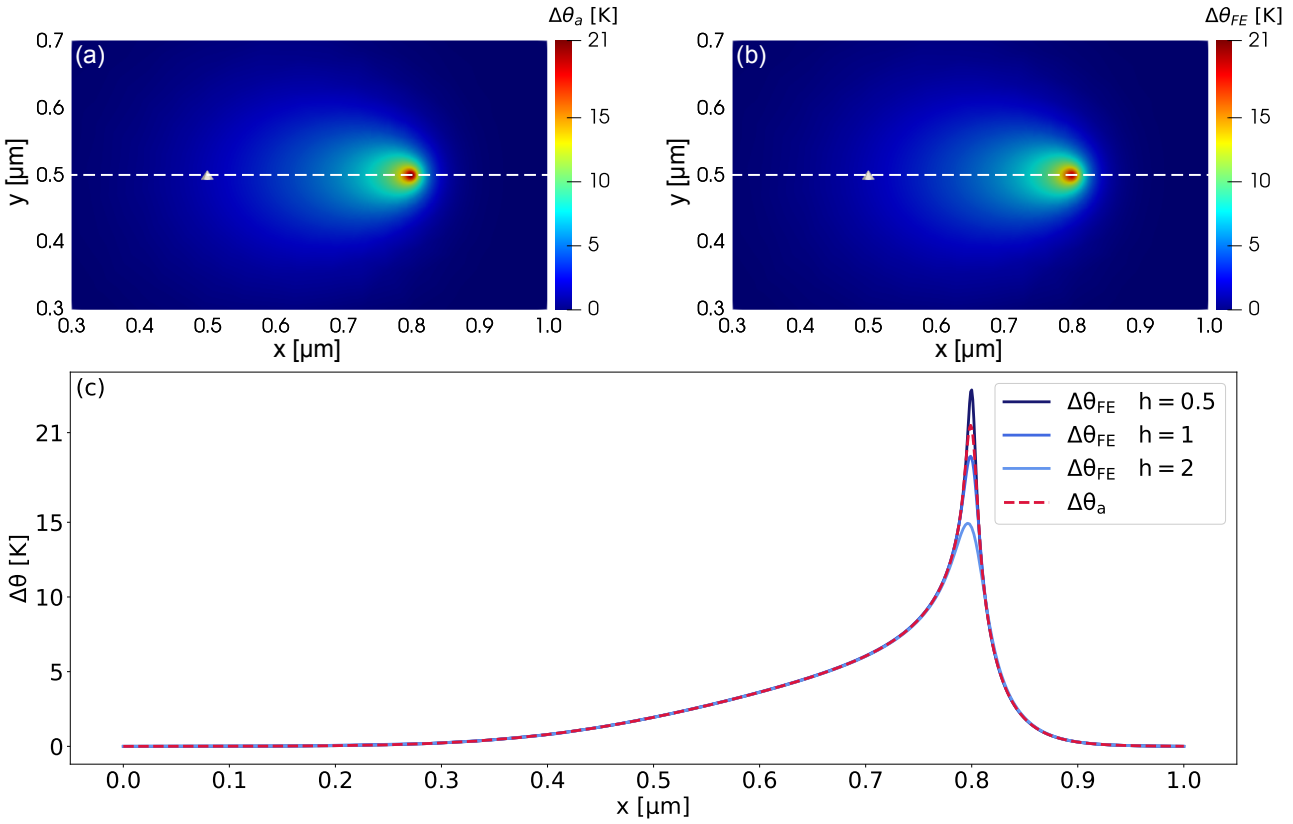

Figure 1: (a) Temperature field computed with the analytical solution ($\Delta\theta_a$); (b) Temperature field computed with the TFDM model ($\Delta\theta_{\text{FE}}$) for $h = 1$ nm and $r_c = 4$ nm. The white triangles in (a) and (b) indicate the dislocation core position at $t = 0$; (c) Line plots of the temperature profiles at $y = 0.5$ μm (dashed lines on (a) and (b)) computed analytically and with the FE implementation for different mesh sizes.

5.2. Illustrative examples

In this section, the temperature evolution due to the transport of edge and screw dislocations, the annihilation of two oppositely-signed edge dislocations, and the expansion of a polygonal loop are studied.

5.2.1. Transport of edge and screw dislocations

In what follows, the temperature profile generated due to the motion of an edge and a screw dislocation are studied while taking into account the heterogeneity of the stress state around the dislocation core; note that in Section 5.1, the stress heterogeneity and coupling with elasticity were neglected for the comparison. The domain, temperature profile, and thermal boundary conditions are the same as in Section 5.1. The initial non-zero dislocation density components for the edge and screw dislocation simulations are $\alpha_{13}^{p(0)}$ and $\alpha_{33}^{p(0)}$, respectively, where both are given by Eq. 5.3. The SSPRK3 scheme is used to solve the dislocation transport Eq. 4.3. For the mechanical problem Eq. 4.6, $\boldsymbol{u} = 0$ is assigned to the plane $y = 0$. A constant dislocation velocity $\boldsymbol{v} = 0.01\,\hat{\boldsymbol{e}}_1$ is assigned. The corresponding constant traction τ given by Eq. 5.1 (around 2 MPa) is applied on the plane $y = 1$ along the x and z directions for the edge and screw dislocation simulations, respectively. Even though the external traction is not driving the dislocation motion, it nevertheless ensures a non-negative global dissipation (Eq. 3.2). The relevant parameters considered in this simulation are shown in Table 1.

The mesh size on the structured region where dislocation motion takes place is $h = 2$ nm. The CFL condition Eq. 5.4 in this case imposes a maximum time step of $\Delta\tilde{t}_{CFL} = 100$, and the chosen time step is $\Delta\tilde{t} = 10$ or $\Delta t = 3.36 \times 10^{-12}$ s. The simulation is run for 5500 time steps.

The simulation results for the edge dislocation are shown in Fig. 2. The stress tensor of the edge dislocation contains diagonal (hydrostatic) components, which are in this case compressive (negative) above the dislocation line and tensile (positive) below it. This is exemplified by the σ_{xx} component evolution in Fig. 2b, d and f. With a motion in the positive x-direction, above the dislocation line, the region ahead of it is locally compressed, while the region behind it is decompressed. This entails a local temperature increase and decrease in these regions, respectively. The opposite reasoning might be applied below the dislocation line, where the region ahead of it undergoes tension, while the region behind it is relaxed from tension, which promotes a local temperature decrease and increase in these regions, respectively. This is the expected thermoelastic effect,

which is present in the model through the third term on the left-hand side of Eq. 4.7 and is well captured by it (Fig. 2c and e). In Fig. 2e, the asymmetry in the extent of the temperature change ahead of and behind the dislocation line is explained by the accommodation of the constant reference temperature boundary condition when it approaches the surface on the right. The temperature variation due to a single edge dislocation moving at $0.01 v_s$ is of the order of 1 mK.

The temperature evolution due to the motion of a screw dislocation is shown in Fig. 3. Similar to the case of edge dislocation, localized cooling and heating also occur. However, the temperature profile evolution is different, and so are the magnitudes of the temperature changes around the core of the edge and the screw dislocations, with a difference of approximately one order of magnitude. To understand this difference, consider the two sources of temperature evolution in Eq. 3.1j, the thermoelastic effect, $\theta\boldsymbol{\beta} : (\nabla\dot{\boldsymbol{u}} - \dot{\boldsymbol{U}}^p) = \theta\beta_{ij}\left((\nabla\dot{u})_{ij} - \dot{U}^p_{ij}\right)$, and the plastic dissipation, $\boldsymbol{\sigma} : \dot{\boldsymbol{U}}^p = \sigma_{ij}\dot{U}^p_{ij}$ (other sources are not taken into account). For isotropic elasticity, the tensor $\boldsymbol{\beta}$ is given by $\beta_{ij} = \gamma(3\lambda + 2\mu)\,\delta_{ij}$. Thus, the thermoelastic source is expressed as

$$\theta\gamma(3\lambda + 2\mu)(\nabla\dot{u})_{ii}\,, \tag{5.5}$$

since $\dot{U}^p_{ii} = 0$. For the screw dislocation α^p_{33}, the only nonzero component of the plastic distortion tensor rate is $\dot{U}^{p,S}_{32} = \alpha^p_{33} v_1$; note that the superscript 'S' corresponds to screw. The plastic dissipation in this case is $\sigma^S_{32}\alpha^p_{33} v_1$. Note that, since α^p_{33} and v_1 are strictly positive (see Eq. 5.3), the sign of the plastic dissipation is dictated by the sign of σ^S_{32}. The closed-form solution for σ^S_{32} is (Hirth & Lothe (1982))

$$\sigma^S_{32} = \frac{\mu b}{2\pi}\frac{x - x_c}{(x - x_c)^2 + (y - y_c)^2}\,,$$

showing that, for $x < x_c$, i.e. on the left of the dislocation line, $\sigma^S_{32} < 0$, whereas $\sigma^S_{32} > 0$ for $x > x_c$, which also applies for the plastic dissipation, as can be seen in Fig. 4a. With the choice of a constant dislocation velocity $\boldsymbol{v}$, a locally negative plastic dissipation is obtained at $x < x_c$. However, the non-negativity of the global dissipation (Eq. 3.2) is ensured at all times. The components of the total displacement of the screw dislocation α^p_{33} are $\boldsymbol{u}^S = [0, 0, u_3(x, y)] \implies (\nabla\dot{u}^S)_{ii} = 0$. Thus, the thermoelastic source in Eq. 5.5 is zero for the screw dislocation (see Fig. 4c). In that case, plastic dissipation is the only source of heat driving the temperature evolution, giving rise to the specific profile shown in Fig. 3b and c. The dislocation motion occurs in the direction of positive plastic dissipation, such that the heat accumulation in front of the dislocation line results in a more substantial temperature increase than the decrease located behind the line, ultimately resulting in an average temperature increase of the body.

For the edge dislocation α^p_{13}, the nonzero component of the plastic distortion tensor rate is $\dot{U}^{p,E}_{12} = \alpha^p_{13} v_1$, which results in the plastic dissipation $\sigma^E_{12}\alpha^p_{13} v_1$; note that the superscript 'E' corresponds to edge. Similar to the screw dislocation case, the sign of the plastic dissipation is determined by the stress component σ^E_{12}, which results in the profile shown in Fig. 4b. The components of the total displacement of the edge dislocation α^p_{13} are $\boldsymbol{u}^E = [u_1(x, y), u_2(x, y), 0] \implies (\nabla\dot{u}^E)_{ii} \neq 0$. Thus, for the edge dislocation, the thermoelastic source of heat (Eq. 5.5) also plays a role in the temperature evolution and is shown in Fig. 4d. The thermoelastic source has an antisymmetric profile about the x and y axis, which gives rise to the temperature profile in Fig. 2c and e, and translates the thermoelastic effect mentioned earlier in this section. The magnitude of the thermoelastic source is around three times greater than that of the plastic dissipation source for the edge dislocation, which shows that the temperature evolution around the core of the edge dislocation is mainly due to the thermoelastic effect (local volume change) close to the core. This also explains the difference between the temperature profiles of the edge and screw dislocations, since, for the latter, only plastic dissipation promotes temperature evolution around the core, resulting in a smaller temperature variation due to the smaller magnitude of the dissipation source when compared to the thermoelastic one, predominant for the edge dislocation. Note that, since the thermoelastic source is antisymmetric, it produces the same magnitude of heating and cooling around the core of the edge dislocation. However, the plastic dissipation also contributes to the temperature evolution, through a mechanism similar to the one described for the screw dislocation. Thus, the motion of the edge dislocation also results in an average increase of the temperature in the domain.

This result is in contrast to the conclusion in Gurrutxaga-Lerma (2017). There, it is stated that plastic dissipation is the only relevant source of heat due to the motion of an edge or a screw dislocation, whereas the present work clearly shows a more pronounced influence of the thermoelastic source of heat when compared to plastic dissipation in the motion of an edge dislocation. This discrepancy arises from the statement of the mechanical problem in Gurrutxaga-Lerma (2017). There, the elastic strain is defined as $\boldsymbol{\varepsilon}^e = \mathrm{sym}(\nabla\boldsymbol{u}) - \boldsymbol{\varepsilon}^\theta$, where $\boldsymbol{\varepsilon}^\theta = \gamma\Delta\theta\,\mathbb{1}$, such that the contribution of the dislocation through the plastic strain is not considered. Instead, the injection and motion of an edge dislocation are accounted for through the definition of a Heaviside step function boundary condition on the component of the total displacement vector $\boldsymbol{u}$ along the Burgers vector direction. In the current work, however, the presence of the dislocation is directly taken into account through the plastic distortion $\boldsymbol{U}^p$ in the definition of the total displacement $\boldsymbol{u}$ (see Eqs. 3.1a to 3.1d, 3.1h and 3.1i). Therefore, the thermoelastic heat source (Eq. 5.5) takes into account the internal stress state due to the dislocation, and comes out to be more significant than the plastic dissipation source in the case of the edge dislocation illustrated here.

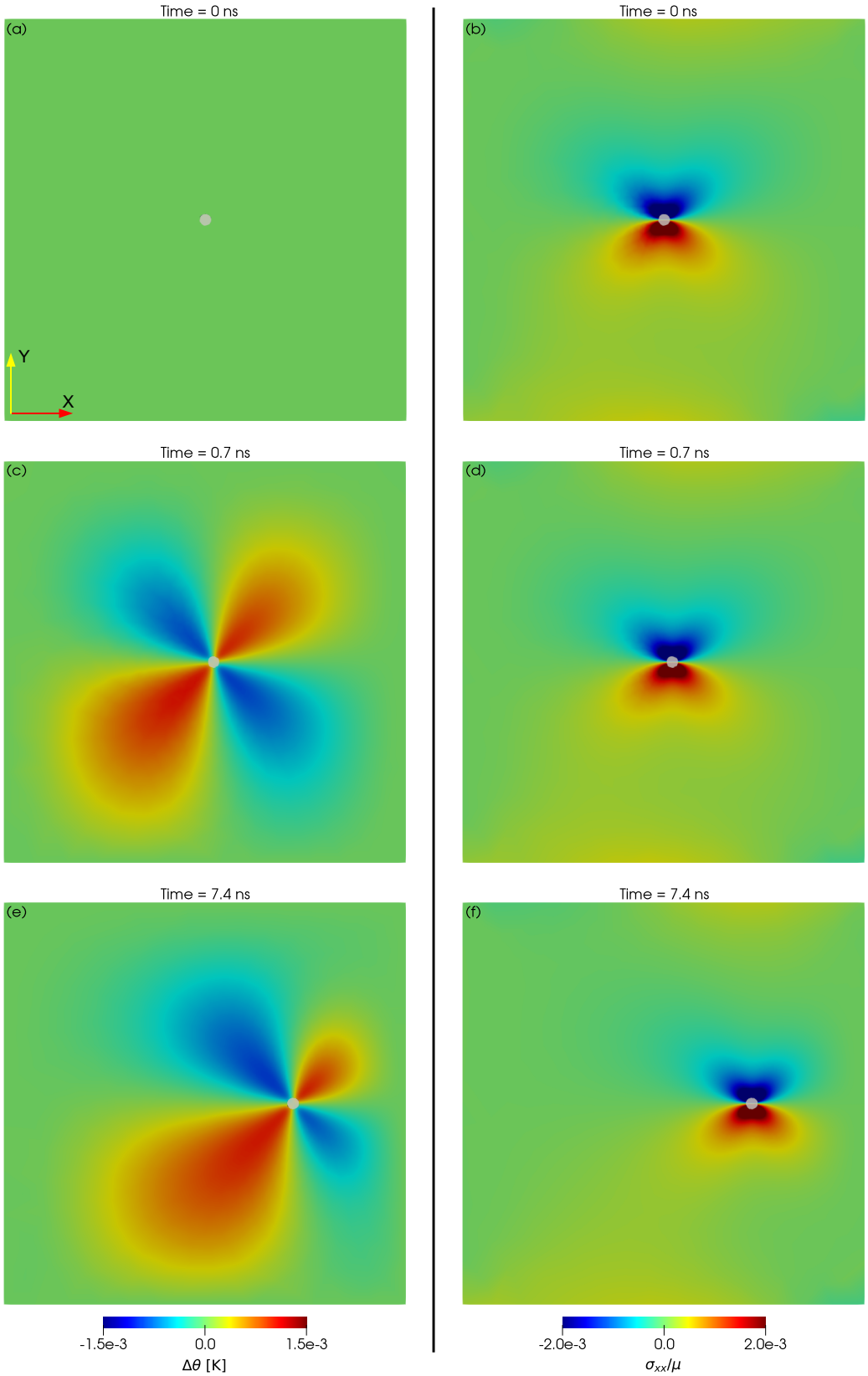

Figure 2: Temperature field generated around the core of an edge dislocation due to its motion in a (1×1) µm^2 domain. The white circles indicate the position of the dislocation core and are localized by the threshold $\left(\alpha^p_{ij}\alpha^p_{ij}\right)^{1/2} > 10^{-4}$. (a), (c) and (e) show the temperature profile evolution and (b), (d), and (f) the σ_{xx} component of the stress tensor evolution, with the corresponding colour bars at the bottom of each column.

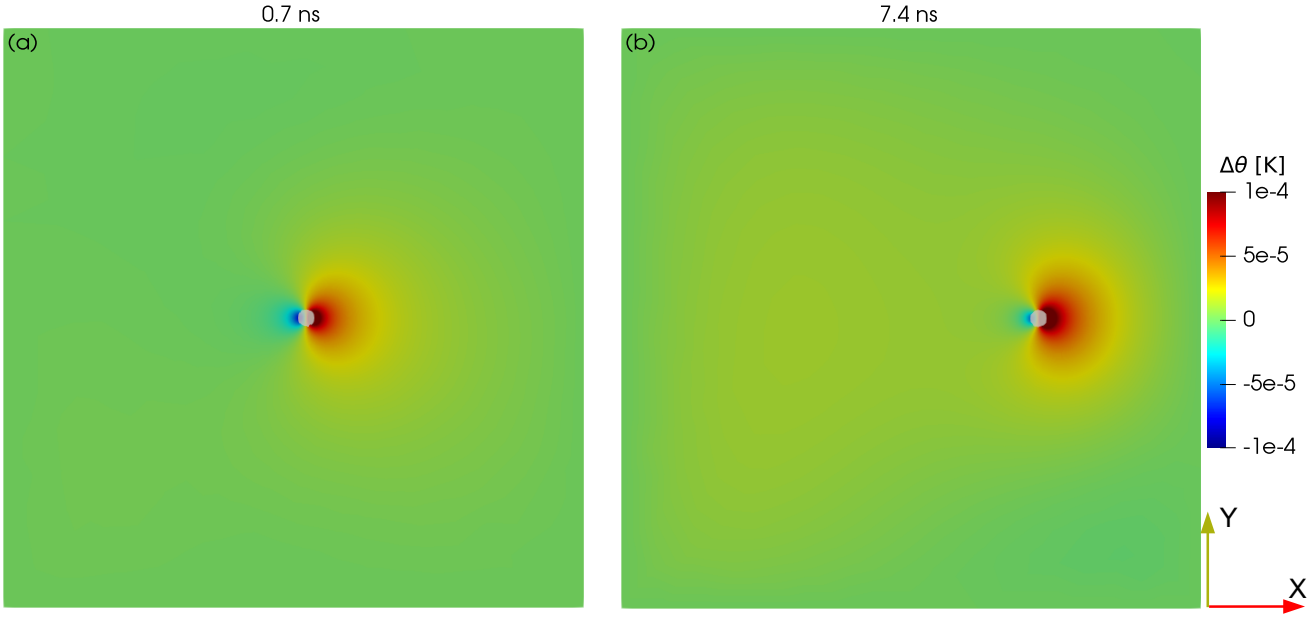

Figure 3: (a) - (b): Temperature field generated around the core of a screw dislocation due to its motion in a (1×1) µm^2 domain. The white circles indicate the position of the dislocation core and are localized by the threshold $\left(\alpha^p_{ij}\alpha^p_{ij}\right)^{1/2} > 10^{-4}$. The same colour bar applies for all surface plots.

5.2.2. *Annihilation of two oppositely signed edge dislocations*

Consider two edge dislocations of opposite signs, whose initial dislocation density is given by

$$\alpha^{p(0)}_{13} = \begin{cases} \phi_0 & |x - x^c_1| \leq r_c \text{ and } |y - y^c_1| \leq r_c \\ -\phi_0 & |x - x^c_2| \leq r_c \text{ and } |y - y^c_2| \leq r_c \\ 0 & \text{otherwise,} \end{cases} \tag{5.6}$$

where (x^c_1, y^c_1) and (x^c_2, y^c_2) are the positions of the centre of each edge dislocation core, and ϕ_0 and r_c are defined as for Eq. 5.3. A structured and refined mesh is used in the region where dislocation motion occurs, with an element size of $h = 1$ nm. The values of the constants in Eq. 5.6 are $(x^c_1, y^c_1) = (0.31, 0.50)$ µm, $(x^c_2, y^c_2) = (0.69, 0.50)$ µm, $r_c = 6$ nm and $\phi_0 = 1.7 \times 10^{-3}$.

The dislocation velocity field considered is

$$\boldsymbol{v} = \left(0.01\text{sign}(\alpha^p_{13})\right)\hat{\boldsymbol{e}}_1, \tag{5.7}$$

such that the dislocation lines will move towards each other with a constant speed of $0.01v_s$. The SSPRK3 scheme is used to compute the dislocation density evolution. The boundary conditions and initial temperature profile are the same as those used in Section 5.2.1, and the parameters in Table 1 are also adopted here. The CFL condition Eq. 5.4 imposes a maximum time step of $\Delta\tilde{t}_{CFL} = 50$, such that the time step considered is $\Delta\tilde{t} = 5$, or $\Delta t = 1.68 \times 10^{-11}$ s, and the simulation is run for 5800 time steps.

The simulation results are shown in Fig. 5 with the initial condition shown in Fig. 5a. In Fig. 5b, a temperature profile similar to the one in Fig. 2e is observed, which is mainly driven by the thermoelastic source of heat Eq. 5.5. As shown in Fig. S2a and b, the thermoelastic heat sources are the same for both dislocation lines, which leads to similar temperature profiles. Upon approximation, regions of opposite $\Delta\theta$ sign tend to neutralize each other, as in Fig. 5b. The curves depicted in Fig. 5d show that the contribution of the plastic dissipation to the temperature evolution increases as the dislocation lines approach each other, due to the increased stress values around the cores. This leads to a localized temperature increase in that region, since the positive parts of the plastic dissipation profile superpose between the dislocation lines (see Fig. S2c and d), hence the more substantial temperature increase shown in Fig. 5c when compared to the single dislocation case (Fig. 2c). Finally, after annihilation occurs, no more heat sources are left in the body, so it returns to the reference temperature.

5.2.3. *Expansion of a polygonal dislocation loop*

Consider a polygonal dislocation loop whose Burgers vector lies in the xy-plane, with density given by $\boldsymbol{\alpha}^p = \alpha^p_{11}\,\hat{\boldsymbol{e}}_1 \otimes \hat{\boldsymbol{e}}_1 + \alpha^p_{12}\,\hat{\boldsymbol{e}}_1 \otimes \hat{\boldsymbol{e}}_2$. The domain size is $(100 \times 100 \times 100)$ nm^3. The mesh is fine and structured (element size $h = 1.29$ nm) in a

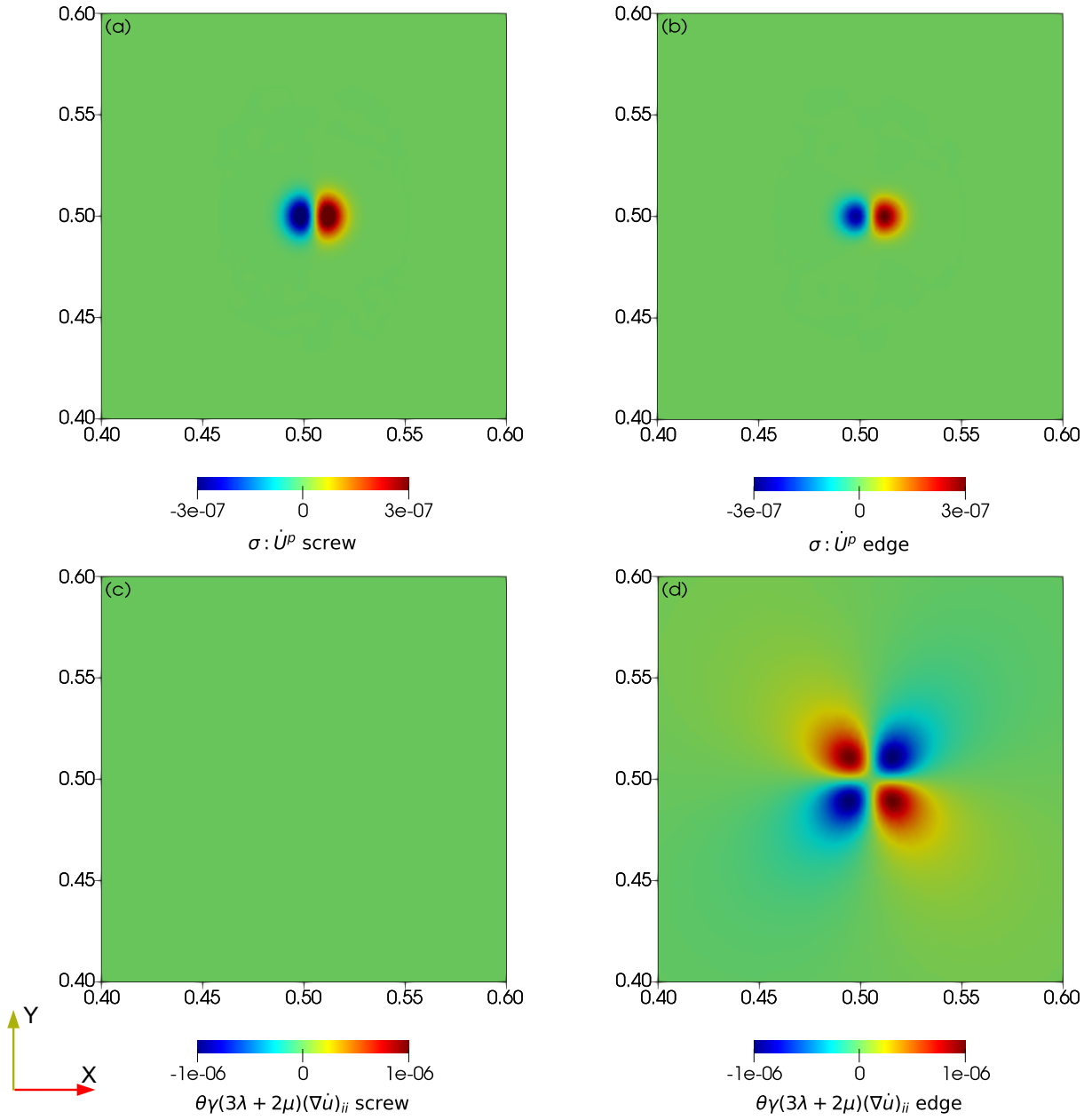

Figure 4: Different sources of heat for edge and screw dislocations. The dimensions are in μm, and the plots are zoomed in the centre of the (1×1) μm^2 shown in Figs. 2 and 3. Plastic dissipation due to the motion of (a) a screw dislocation and (b) an edge dislocation. Thermoelastic heat source generated by the motion of (c) a screw dislocation and (d) an edge dislocation.

rectangular cuboid region of $(100 \times 100 \times 9)$ nm^3 centred at $(50, 50, 50)$ nm, and coarser and unstructured elsewhere, as shown in Fig. S3.

The initial dislocation loop configuration is shown in Fig. 6a. The loop is centered at $(50, 50, 50)$ nm, and its side length is $L = l_c + 2w_c$, where $l_c = 10h$ is the length of the straight segments, and $w_c = 4h$ is the core width. The straight screw and edge segments have an initial density $\alpha_{11}^{p(0)} = \phi_0$ and $\alpha_{12}^{p(0)} = \phi_0$ on the bottom and on the right, and $\alpha_{11}^{p(0)} = -\phi_0$ and $\alpha_{12}^{p(0)} = -\phi_0$ on the top and the left of the loop, respectively. On the corners of the loop, the initial densities are

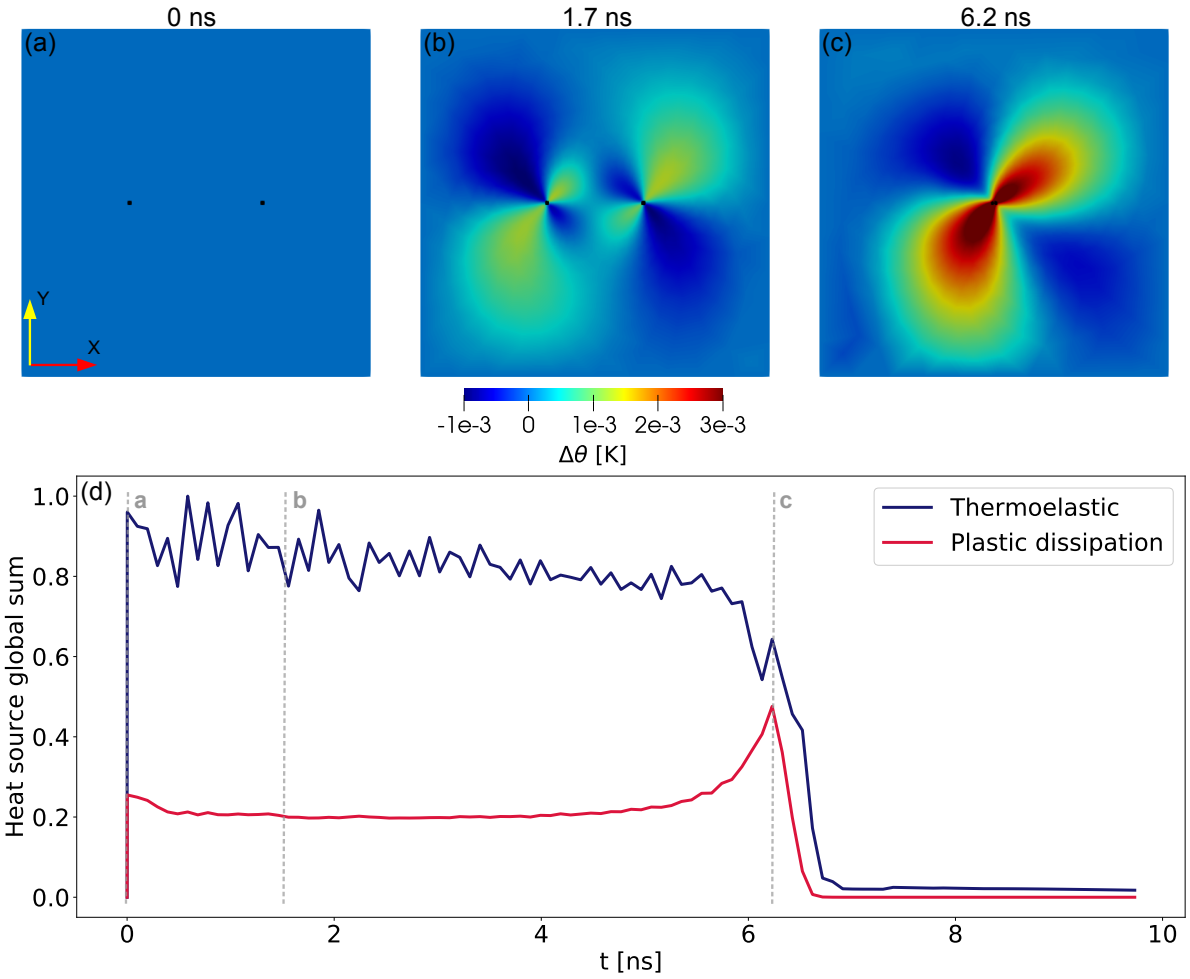

Figure 5: (a) - (c): Temperature field evolution during the annihilation of two oppositely signed edge dislocations in a (1×1) μm^2 domain. The black squares indicate the positions of the dislocation cores, localized by the threshold $\left(\alpha^p_{ij}\alpha^p_{ij}\right)^{1/2} > 10^{-3}$, and the colour bar applies to all surface plots. (d) Evolution of the maximum absolute value of the plastic dissipation and thermoelastic heat sources, normalized by the maximum value of the latter. The grey dashed lines indicate the times corresponding to the snapshots in (a) - (c).

$$\begin{aligned}
\alpha^{p(0)}_{11} &= -\phi_0 \frac{y - (y_c + b)}{\sqrt{\left(x - (x_c + a)\right)^2 + \left(y - (y_c + b)\right)^2}} \\
\alpha^{p(0)}_{12} &= \phi_0 \frac{x - (x_c + a)}{\sqrt{\left(x - (x_c + a)\right)^2 + \left(y - (y_c + b)\right)^2}},
\end{aligned} \tag{5.8}$$

where $(x_c, y_c) = (50, 50)$ nm are the coordinates of the centre of the loop, (a, b) are equal to (l_c, l_c), $(-l_c, l_c)$, $(-l_c, -l_c)$, $(l_c, -l_c)$ on the top right, top left, bottom left and bottom right corners of the loop, respectively, and $\phi_0 = 1.03 \times 10^{-1}$. The dislocation velocity is assigned to be normal to the line segments, with components on the xy-plane given by

$$\begin{aligned}
v_1 &= v_0 \frac{\alpha^p_{12}}{\|\boldsymbol{\alpha}^p\|} \\
v_2 &= -v_0 \frac{\alpha^p_{11}}{\|\boldsymbol{\alpha}^p\|} \\
\|\boldsymbol{\alpha}^p\| &= \sqrt{\left(\alpha^p_{11}\right)^2 + \left(\alpha^p_{12}\right)^2},
\end{aligned} \tag{5.9}$$

where $v_0 = 0.01 v_s$ is constant. The SSPRK2 scheme is used to compute the dislocation density evolution. For this simulation, $\boldsymbol{u} = 0$ is imposed on the $z = 0$ plane, and the use of Eq. 5.1 for the boundary traction value results in a negative dissipation of the model, given by Eq. 3.2. Thus, an arbitrary traction value $t = -1$ GPa is applied on the $z = 100$ plane along the x-direction to ensure a non-negative global dissipation (Eq. 3.2). A constant temperature $\theta = \theta_0$ is imposed on all boundaries. The parameters shown in Table 1 are also used here. The CFL condition Eq. 5.4 allows for a maximum time step of $\Delta\tilde{t}_{CFL} = 64.5$ and the time step used is $\Delta\tilde{t} = 1$ or $\Delta t = 3.36 \times 10^{-13}$ s.

The simulation result is depicted in Fig. 6. Due to the arbitrariness of the applied traction value, no quantitative information can be extracted from the temperature values, hence the normalization depicted in the colour bar of Fig. 6d. As can be seen in Eq. 5.5, the thermoelastic heat source is dependent only on the rate of the total distortion tensor $\nabla\dot{\boldsymbol{u}}$, which is computed as $\nabla\dot{\boldsymbol{u}} = \left(\nabla\boldsymbol{u}^{n+1} - \nabla\boldsymbol{u}^{n}\right)/\Delta t$, such that the influence of the applied tractions is removed (provided that these remain constant). Thus, dislocation motion is the only one contributing to the evolution of $\nabla\boldsymbol{u}$ by altering the displacement field according to the position of the dislocation line. Consequently, for a given domain, initial dislocation configuration and dislocation evolution, the thermoelastic heat source remains constant regardless of changes in the mechanical boundary conditions. This is not the case for the plastic dissipation heat source $\boldsymbol{\sigma} : \dot{\boldsymbol{U}}^p$, as it is dependent on the stress state that comprises contributions both from the applied tractions and the loop. Since in this simulation the value of the applied traction t was significantly increased with respect to the single dislocation and annihilation cases (1 GPa vs. 2 MPa), the plastic dissipation heat source became dominant over the thermoelastic one (about one order of magnitude higher) for the edge components of the dislocation loop. Therefore, the temperature profile is governed by plastic dissipation, as shown in the evolution of the global sum of heat sources in Fig. 6e.

At the beginning of the simulation, the plastic dissipation profile is akin to Fig. 4a and b, with positive and negative parts of similar magnitude, as can be seen at the dashed line b of Fig. 6e. This leads to a comparable temperature increase and decrease outside and inside dislocation loop, respectively. As the loop expands and approaches the boundaries of the domain, the positive part of the plastic dissipation increases due to the appearance of free surface effects, which distorts and increases the magnitude of the stress component that drives the dissipation (σ_{13}, in this case), as depicted in Fig. 6e. This results in a predominance of the temperature increase in the domain when compared to the decrease promoted by the negative part of the plastic dissipation, as shown in Fig. 6c and d. The point of maximum plastic dissipation occurs when the core of the dislocation loop reaches the boundary of the domain, Fig. 6d. After the loop exits the body, there are no heat sources left, so the system returns to the reference temperature.

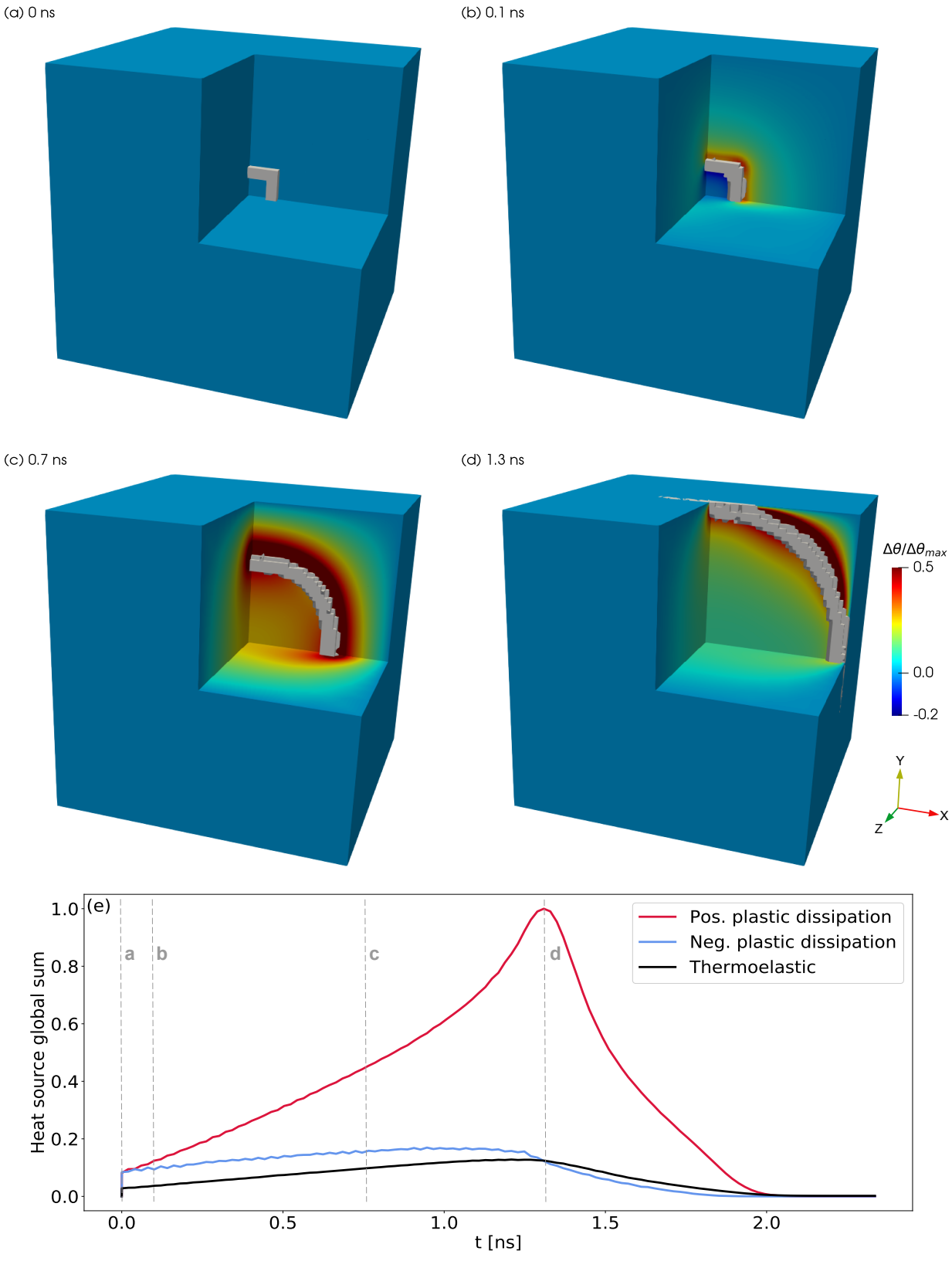

Figure 6: (a) - (d) Temperature field evolution on the planes $x = 50$ nm, $y = 50$ nm, and $z = 50$ nm during the expansion of a polygonal dislocation loop in a $(100 \times 100 \times 100)$ nm^3 domain. The loop is shown in grey and is localized by the threshold $\left(\alpha^p_{ij}\alpha^p_{ij}\right)^{1/2} > 10^{-2}$. The temperature is normalized with respect to its maximum value, and the same colour bar applies to all surface plots. (e) Sum over the domain of the absolute values of the thermoelastic and plastic dissipation heat sources' evolution during the loop expansion simulation. The positive and negative components of the dissipation are plotted separately, and all curves are normalized by the maximum value of the positive plastic dissipation. The grey dashed lines indicate the times corresponding to the snapshots in (a) - (d)

6. Conclusion and perspectives

This paper presents the FE approximation of the fully coupled TFDM (thermal field dislocation mechanics) model (Upadhyay (2020)). The variational formulations of the TFDM governing equations are presented and a staggered numerical algorithm for their resolution is proposed. In addition to all the possibilities of the isothermal FDM model, the TFDM model allows for explicitly modelling the influence of dislocation activity on the temperature profile evolution of a body as well as the influence of temperature and heat flux boundary conditions on dislocation evolution.

The TFDM-FE model is validated by comparison with an analytical solution of the temperature profile generated due to the motion of a single edge dislocation in a constant homogeneous stress field neglecting the dislocation self-stress. A remarkable agreement is obtained between the analytical and numerical solutions outside the dislocation core. The solutions differ within the dislocation core due to the difference in the manner in which the dislocations are treated in the analytical solution (singular defect) and the TFDM-FE model (a finite non-zero polar density). A mesh convergence analysis demonstrated the improvement of the match between the two approaches.

Following this validation, the model is applied to study the transport of edge and screw dislocations, dislocation annihilation and expansion of a polygonal loop. In all these simulations, the heterogeneity of the stress state around the core of the dislocations is considered. The analysis of the temperature profile evolution during the motion of an edge and a screw dislocation showed that the thermoelastic coupling and the plastic dissipation contribute differently according to the dislocation type. For an edge dislocation studied here, the thermoelastic effect is found to have the highest contribution to temperature evolution, whereas plastic dissipation is the only active heat source during transport of a screw dislocation. The dislocation annihilation reveals an increasing influence of plastic dissipation on the temperature evolution due to the increase in the stresses near the dislocation cores as the dislocations approach each other. An increasing influence of plastic dissipation also occurs in the dislocation loop expansion case due to the increasing effect of image stresses from domain boundaries.

Acknowledgments

The authors are grateful to the European Research Council (ERC) for their support through the European Union's Horizon 2020 research and innovation program for project GAMMA (Grant agreement No. 946959).

Declaration of interests

The authors declare that they have no known competing financial interests or personal relationships that could have appeared to influence the work reported in this paper.

References

Acharya, A. (2001). A model of crystal plasticity based on the theory of continuously distributed dislocations. *Journal of the Mechanics and Physics of Solids*, *49*, 761–784. URL: https://www.sciencedirect.com/science/article/pii/S0022509600000600. doi:https://doi.org/10.1016/S0022-5096(00)00060-0.

Acharya, A. (2003). Driving forces and boundary conditions in continuum dislocation mechanics. *Proceedings of the Royal Society of London. Series A: Mathematical, Physical and Engineering Sciences*, *459*, 1343–1363.

Acharya, A. (2011). Microcanonical Entropy and Mesoscale Dislocation Mechanics and Plasticity. *Journal of Elasticity*, *104*, 23–44. URL: http://link.springer.com/10.1007/s10659-011-9328-3. doi:10.1007/s10659-011-9328-3.

Acharya, A., & Roy, A. (2006). Size effects and idealized dislocation microstructure at small scales: Predictions of a Phenomenological model of Mesoscopic Field Dislocation Mechanics: Part I. *Journal of the Mechanics and Physics of Solids*, *54*, 1687–1710. URL: https://linkinghub.elsevier.com/retrieve/pii/S0022509606000238. doi:10.1016/j.jmps.2006.01.009.

Djaka, K. S., Taupin, V., Berbenni, S., & Fressengeas, C. (2015). A numerical spectral approach to solve the dislocation density transport equation. *Modelling and Simulation in Materials Science and Engineering*, *23*, 065008. URL: https://iopscience.iop.org/article/10.1088/0965-0393/23/6/065008. doi:10.1088/0965-0393/23/6/065008.

Gurrutxaga-Lerma, B. (2017). How strong is the temperature increase due to a moving dislocation?, . *108*, 263–274. URL: https://www.sciencedirect.com/science/article/pii/S0020768316304103. doi:10.1016/j.ijsolstr.2016.12.026.

Hirth, J. P., & Lothe, J. (1982). *Theory of dislocations*. (2nd ed.). New York: Wiley.

Kosevich, A. M. (1979). Crystal dislocations and the theory of elasticity. In F. R. N. Nabarro (Ed.), *Dislocations in solids* (pp. 33–141). Amsterdam New York Oxford: North-Holland publ.

Logg, A., Mardal, K.-A., & Wells, G. (Eds.) (2012). *Automated Solution of Differential Equations by the Finite Element Method: The FEniCS Book*. Number 84 in Lecture Notes in Computational Science and Engineering. Heidelberg: Springer.

Mura, T. (1963). Continuous distribution of moving dislocations. *Philosophical Magazine*, *8*, 843–857. URL: http://www.tandfonline.com/doi/abs/10.1080/14786436308213841. doi:10.1080/14786436308213841.

Peach, M., & Koehler, J. S. (1950). The Forces Exerted on Dislocations and the Stress Fields Produced by Them. *Physical Review*, *80*, 436–439. URL: https://link.aps.org/doi/10.1103/PhysRev.80.436. doi:10.1103/PhysRev.80.436.

Roy, A., & Acharya, A. (2005). Finite element approximation of field dislocation mechanics. *Journal of the Mechanics and Physics of Solids*, *53*, 143–170. URL: https://www.sciencedirect.com/science/article/pii/S0022509604001097. doi:10.1016/j.jmps.2004.05.007.

Upadhyay, M. V. (2020). On the thermo-mechanical theory of field dislocations in transient heterogeneous temperature fields. *Journal of the Mechanics and Physics of Solids*, *145*, 104150. URL: https://linkinghub.elsevier.com/retrieve/pii/S0022509620303835. doi:10.1016/j.jmps.2020.104150.

Upadhyay, M. V., & Bleyer, J. (2021). Dislocation transport using a time-explicit runge-kutta discontinuous galerkin finite element approach. *Modelling and Simulation in Materials Science and Engineering*, . URL: http://iopscience.iop.org/article/10.1088/1361-651X/ac44a7.

Varadhan, S. N., Beaudoin, A. J., Acharya, A., & Fressengeas, C. (2006). Dislocation transport using an explicit Galerkin/least-squares formulation. *Modelling and Simulation in Materials Science and Engineering*, *14*, 1245–1270. URL: https://iopscience.iop.org/article/10.1088/0965-0393/14/7/011. doi:10.1088/0965-0393/14/7/011.

Willis, J. (1967). Second-order effects of dislocations in anisotropic crystals. *International Journal of Engineering Science*, *5*, 171–190. URL: https://linkinghub.elsevier.com/retrieve/pii/0020722567900031. doi:10.1016/0020-7225(67)90003-1.

Zhang, X., Acharya, A., Walkington, N. J., & Bielak, J. (2015). A single theory for some quasi-static, supersonic, atomic, and tectonic scale applications of dislocations. *Journal of the Mechanics and Physics of Solids*, *84*, 145–195. URL: https://linkinghub.elsevier.com/retrieve/pii/S0022509615300120. doi:10.1016/j.jmps.2015.07.004.

7. Supplementary material

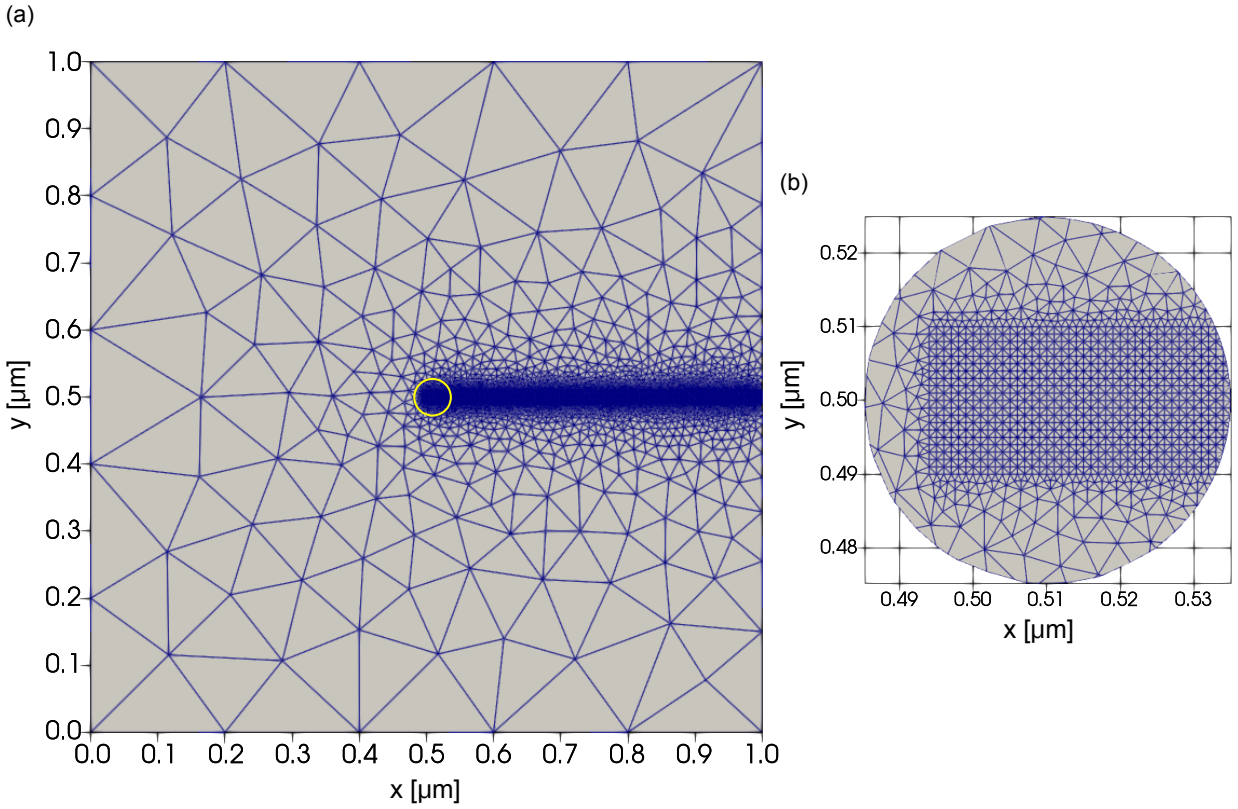

Figure S1: Mesh used for the model validation in Section 5.1. The element size in the structured region is $h = 1$ nm. The yellow circle in (a) indicates the zoomed region depicted in (b).

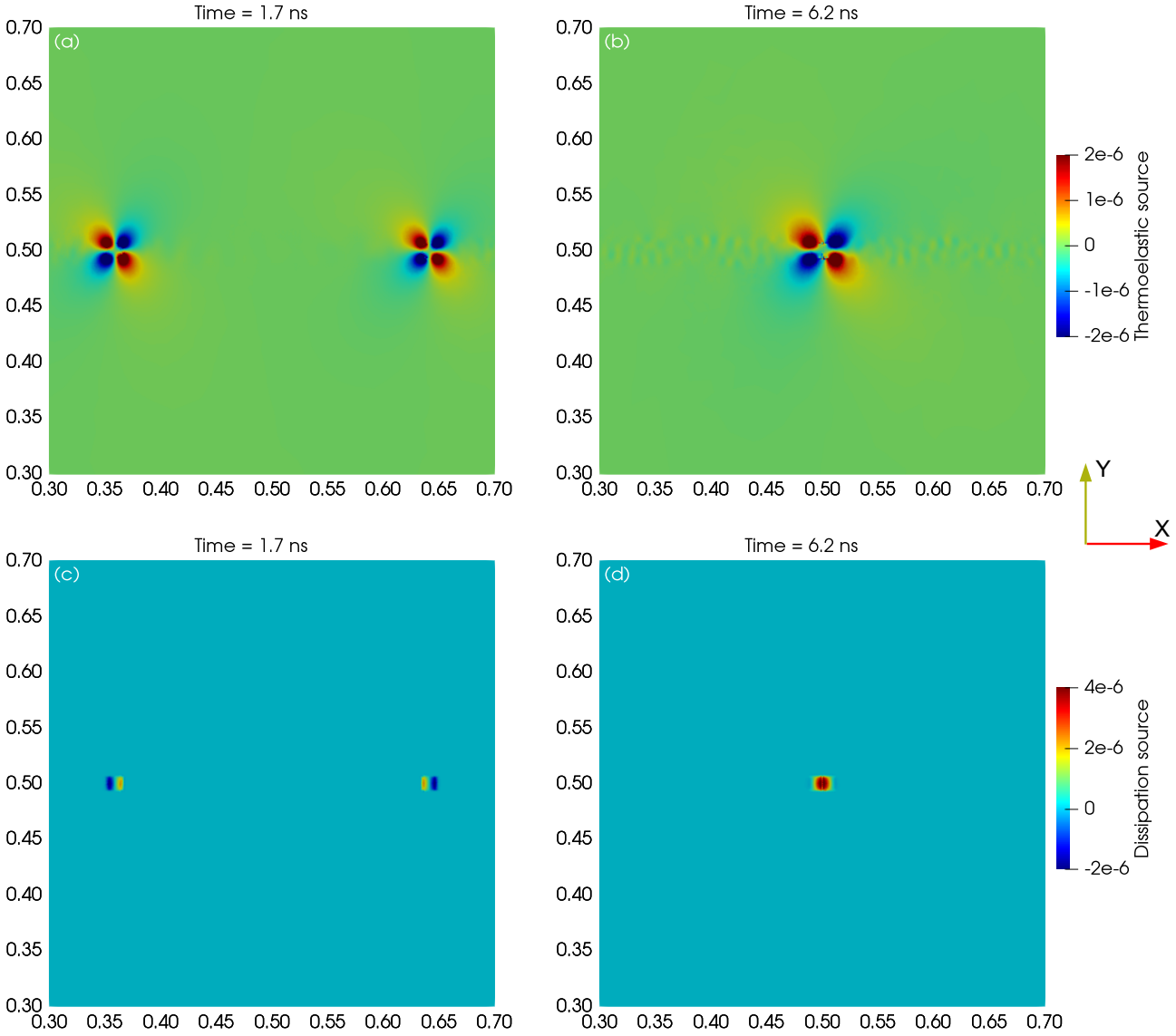

Figure S2: Heat sources evolution during the dislocation annihilation simulation for the time steps depicted in Fig. 5b and c. The dimensions are in µm, and the plots are zoomed in the central region of the (1×1) µm^2 domain of Fig. 5a to c. (a) and (b): thermoelastic heat sources; (c) and (d): plastic dissipation heat sources. The corresponding colour bars are on the right of figures (b) and (d).

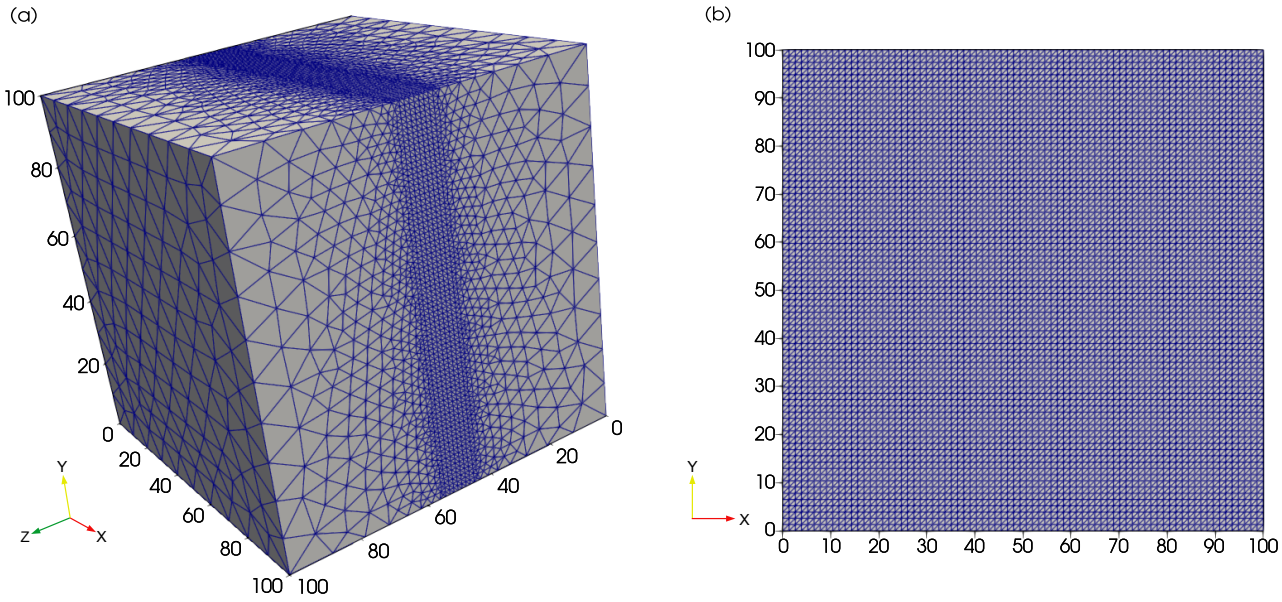

Figure S3: Mesh used for the dislocation loop simulation in Section 5.2.3. (a) 3D perspective showing the structured and unstructured regions; (b) 2D view of the $z = 49.36$ plane showing the structured region where the loop expansion occurs. The dimensions are in nm.